Wall-Modeled LES of a Swept Wing with Leading-Edge Ice Using LAVA Curvilinear, Unstructured, and Cartesian Solvers

David A. Craig Penner*, Victor C. B. Sousa†, Kiran Ravikumar‡, Kumar Saurabh§, Francois Cadieux¶, Gerrit-Daniel Stich‖, Michael F. Barad**, Jeffrey A. Housman††, Jared C. Duensing‡‡
NASA Ames Research Center, Moffett Field, CA 94035

Wall-modeled large-eddy simulation (LES) of a swept wing with leading-edge ice buildup is performed using three mesh paradigms and associated flow solvers and compared to experimental results. The study focuses on an 8.9% scale model of the CRM65 swept wing featuring both high-fidelity and smooth leading-edge ice shapes. The assessment is conducted using the Launch, Ascent, and Vehicle Aerodynamics (LAVA) framework using the three actively supported meshing paradigms in LAVA: structured curvilinear overset, unstructured, and Cartesian. For the iced configurations, these paradigms use hybrid body-fitted/source-term immersed-boundary, body-fitted, and ghost-cell immersed-boundary strategies, respectively. The unstructured and Cartesian mesh paradigms are particularly attractive for complex ice shapes as they avoid the manual mesh generation effort associated with the curvilinear approach. For the high-fidelity ice shape, good agreement with the experiment can be obtained with all three strategies; however, the curvilinear method is particularly sensitive to the source-term immersed-boundary timescale and spanwise mesh resolution, and the Cartesian implementation is sensitive to the choice of numerical flux. For the smooth ice, larger discrepancies are observed across all methods. However, a mesh refinement study guided by flow visualizations leads to an improved comparison with the experiment that is particularly pronounced for the unstructured mesh paradigm.

I. Introduction

UNDERSTANDING the aerodynamic performance effects of ice buildup during flight is important to mitigate the negative impacts of in-flight icing, including reduced lift, nonlinear changes in pitching moment, and increased drag [1]. Computational approaches for understanding iced flows are attractive as they can be financially cheaper and less resource intensive compared to traditional wind tunnel experiments and flight tests. However, iced configurations typically lead to complex flows involving separated regions and a range of length scales that are challenging for numerical methods to capture. Stebbins et al. [2] notes that Reynolds-averaged Navier-Stokes (RANS) methods are commonly used to simulate iced flows (e.g., [3, 4]) due to their relatively cheap computational cost and historical legacy. However, they have difficulty predicting aerodynamic loads for separated flows, which are common for high angles of attack and iced geometries [5–7].

As an alternative to RANS, scale-resolving approaches like wall-modeled large-eddy simulation (WMLES), along with other hybrid approaches, have been introduced as a computationally tractable means of time-accurately resolving large-scale turbulent structures while modeling subgrid-scale features. Xiao et al. [8, 9] performed pioneering work applying WMLES to iced airfoils. They noted the remarkable ability of WMLES to predict flow separation and resolve the Kelvin-Helmholtz instability associated with the ice-induced separated shear layer. Similar results were obtained by Wong et al. [10] for a NACA 23012 airfoil with EG1164 horn ice accretion. This case was also used as a validation test for Voronoi WMLES in [11]. Bornhoft et al. [12] studied a NACA 23012 airfoil with several different ice shapes and observed that WMLES accurately captured the aerodynamics of glaze ice shapes with large roughness scales, but that

*Science and Technology Corporation, AIAA Member, david.a.craigpenner@nasa.gov.
†Science and Technology Corporation, AIAA Member, victor.decarvalhobrittosousa@nasa.gov.
‡Science and Technology Corporation, kiran.ravikumar@nasa.gov.
§Science and Technology Corporation, kumar.saurabh@nasa.gov.
¶Computational Aerosciences Branch, AIAA Member, francois.cadieux@nasa.gov
‖Science and Technology Corporation, AIAA Member, gerrit-daniel.stich@nasa.gov.
**Computational Aerosciences Branch, AIAA Senior Member, michael.f.barad@nasa.gov.
††Computational Aerosciences Branch, AIAA Senior Member, jeffrey.a.housman@nasa.gov.
‡‡Computational Aerosciences Branch, AIAA Member, jared.c.duensing@nasa.gov.

special consideration must be taken for rime ice shapes when the roughness scales are sub-grid. Recent WMLES studies have focused on three-dimensional ice shapes formed on a straight wing with the NACA 23012 airfoil section [13] and an 8.9% scale version of the CRM65 swept wing, a 65% scale version of the Common Research Model (CRM) geometry [11, 14]. Note that the CRM geometry was initially created for the AIAA Drag Prediction Workshop [15–18].

The subscale CRM65 geometry with leading-edge ice accretion is an attractive validation case for numerical methods in part because it has been studied in detail experimentally [19–22]. Numerical studies have focused on two three-dimensional ice shapes: a high-fidelity shape representative of realistic ice accretion and a smooth shape approximating the high-fidelity ice shape by smoothly lofting the local maximum cross-sectional profiles of the high-fidelity ice shape across the wing span. The development and study of the latter shape is due to icing simulation tools that cannot reproduce the high-fidelity shape [23–25]. This test case has been used to evaluate improved delayed detached-eddy simulation [26], RANS [27, 28], and WMLES [11, 14] methods.

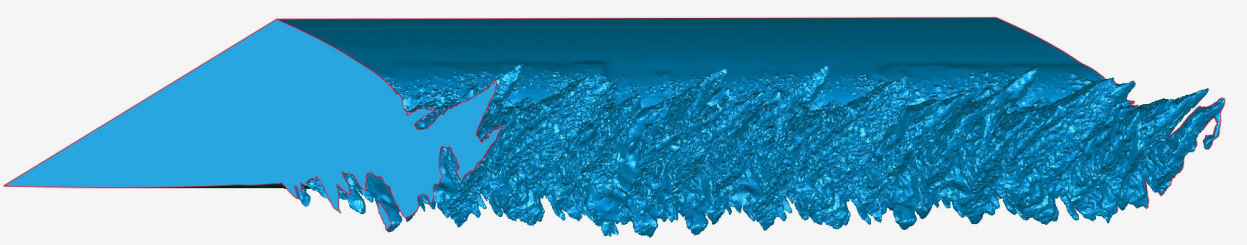
The objective of this work is to evaluate WMLES of the iced CRM65 geometry with all three mesh paradigms within the Launch, Ascent, and Vehicle Aerodynamics (LAVA) framework [29]. This work builds upon [11], which presented results for this case with LAVA curvilinear and unstructured Voronoi paradigms. Specifically, sensitivities with LAVA Curvilinear are addressed which affect accuracy for the high-fidelity ice shape. Also, the moment discrepancy at high angles of attack with LAVA Unstructured is discussed and rectified. For the smooth ice with LAVA Unstructured, flow visualizations are examined leading to judicious construction of finer meshes leading to improved comparison with the experiment. Furthermore, results with LAVA Cartesian for high-fidelity and smooth ice are presented. Notably, the unstructured Voronoi and Cartesian results are generated entirely using GPU-ported versions of those codes, leading to improved simulation turnaround times. Both these solvers have undergone optimizations targeting NVIDIA A100 GPUs and are capable of simulating a problem to the same level of accuracy as the CPU implementations while using only a fraction of the energy. Further discussion about the computational cost can be found in Sozer et al. [30]. Relevant details about the iced CRM65 test case are provided in Sec. II. Subsequently, the computational methodologies for each mesh paradigm and associated solver within LAVA are described in Sec. III, followed by numerical results in Sec. IV. A comparison of results across the three mesh paradigms and solvers leads to conclusions regarding WMLES for iced aerodynamics predictions.

II. Problem Description

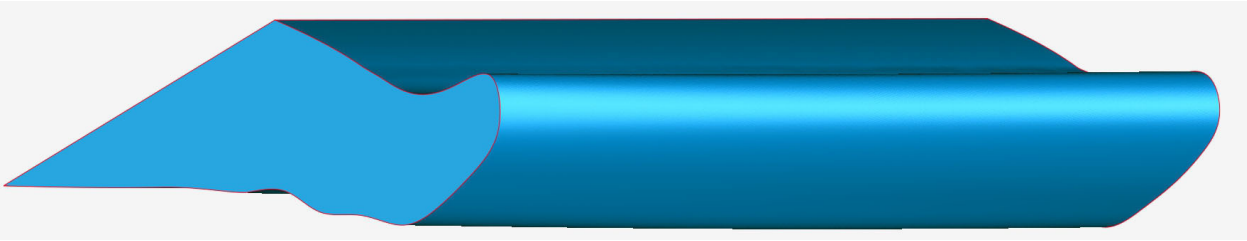
This work investigates the aerodynamic performance of CRM65 wing with high-fidelity and smooth leading-edge ice shapes. These ice shapes were initially conceived in the context of experimental work [20, 21, 23]. To develop them, portions of the wing were placed inside NASA's Glenn Research Center's Icing Research Tunnel at conditions facilitating ice buildup. The resulting ice shapes were then digitized using a laser-scanning procedure, printed using additive manufacturing techniques, and affixed to the leading-edge of a wind tunnel model for experimental data collection. Representative sections of these two ice shapes are shown in Fig. 1. For the ice triangulations, Geomagic Wrap [31] was used to fix the triangulations and make them manifold and these versions of the triangulations were used to obtain the numerical results presented in this paper, as opposed to the shrink-wrapped triangulations used in [11]. However, negligible differences were observed between these two versions of the triangulations in terms of aerodynamic performance. Detailed information about the distinction between the shrink-wrapped and Geomagic-fixed triangulations is given in [11]. The experimental data used in the present work was obtained at the Walter H. Beech Wind Tunnel at Wichita State University (WSU) in Wichita, Kansas [20]. The flow conditions of interest are summarized in Table 1, while Table 2 provides the geometric information for the CRM65 wing. The present work compares aerodynamic loads, surface pressure profiles, and surface oil flow visualizations to LAVA WMLES predictions. For the surface pressure profiles, Fig. 2 and Table 3 detail the pressure tap locations used to collect information about experimental surface pressure distributions.

Table 1 Flow conditions for the iced CRM65 wing.

Name	Symbol	Value
Reynolds number per mean aerodynamic chord	Re	1.6×10^6
Mach number	M	0.18
Freestream dynamic pressure	q_∞	2068.43 Pa (0.3 psi)
Freestream temperature	T_∞	288.87 K
Freestream velocity magnitude	u_∞	$61.34\ \mathrm{m\,s^{-1}}$
Freestream pressure	p_∞	91 200.62 Pa
Freestream density	ρ_∞	$1.10\ \mathrm{kg\,m^{-3}}$
Specific heat of air at constant pressure	c_p	$1005\ \mathrm{J\,kg^{-1}\,K^{-1}}$
Ratio of specific heats	γ	1.4
Sutherland law constant	C_S	$1.45 \times 10^{-6}\ \mathrm{kg\,m^{-1}\,s^{-1}\,K^{-0.5}}$
Sutherland temperature	C	110 K



(a) High-fidelity ice shape



(b) Smooth ice shape

Fig. 1 Renderings of ice shapes from [20] showing representative sections of high-fidelity and smooth leading-edge ice accretions.

Table 2 Summary of geometric parameters for the 8.9% scale CRM65 wing [19, 21, 22].

Wing Parameter	8.9% Scale (WSU Model)	
Span, b	60.00 in	1.524 m
Mean aerodynamic chord, MAC	16.67 in	0.423 m
Area (geometric)	865.3 in^2	0.558 m
Volume	1069 in^3	0.0175 m^3
Aspect ratio*	8.3	
Taper ratio	0.23	
Root chord	27.00 in	0.686 m
Tip chord	6.19 in	0.157 m
Root twist	4.4°	
Tip twist	−3.8°	
Sweep angle (1/4-chord)	35°	
Sweep angle (leading edge)	37.2°	
Location of rotation center†	$x = 19.37$ in, $y = 0$ in, $z = 0$ in	$x = 0.492$ m, $y = 0$ m, $z = 0$ m
Location of moment center†	$x = 23.87$ in, $y = 0$ in, $z = 0$ in	$x = 0.606$ m, $y = 0$ m, $z = 0$ m
Location of MAC (1/4-chord)†	$x = 17.49$ in, $y = 0$ in, $z = 0$ in	$x = 0.444$ m, $y = 0$ m, $z = 0$ m

*Whereas the other parameters in this table are defined specifically for this geometry, the aspect ratio is defined for a full aircraft configuration using the formula $(2 \times \text{semispan})/(2 \times \text{area of one wing})$.

†$(0, 0, 0)$ is the wing root-section leading edge at zero angle of attack.

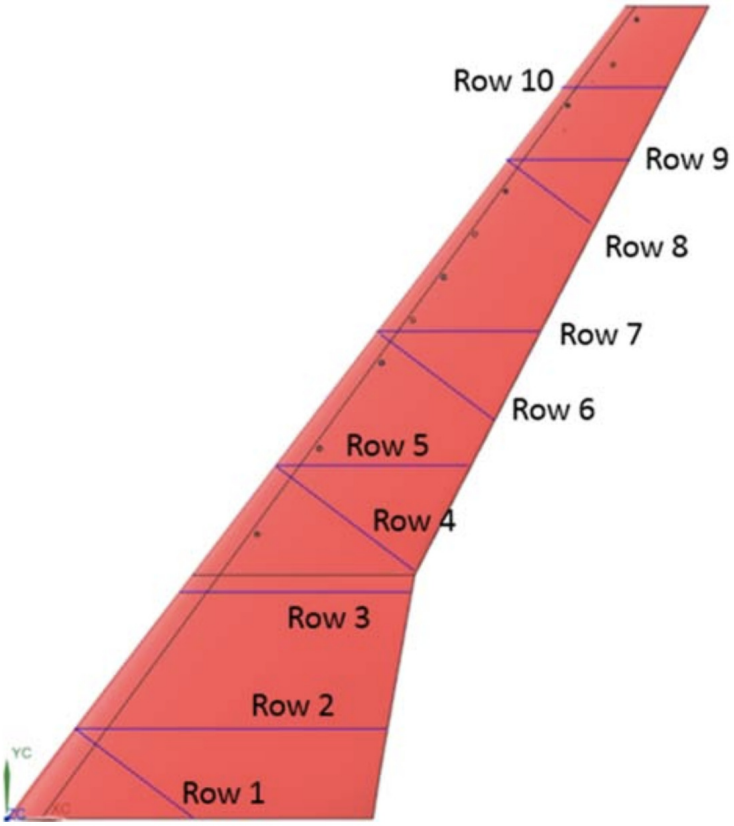
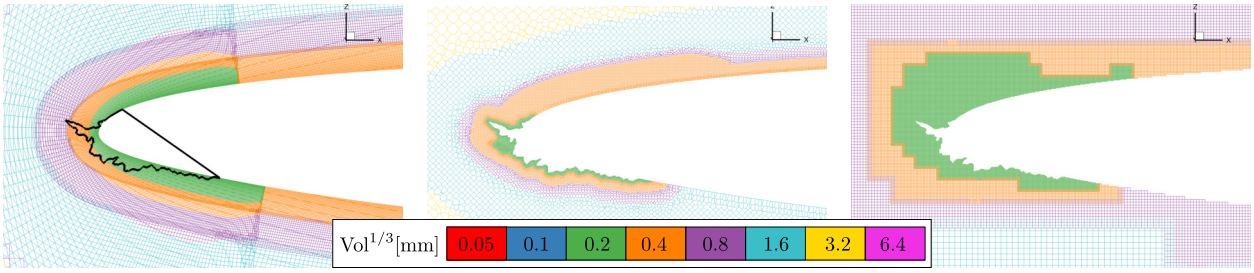


Fig. 2 Pressure tap locations on the 8.9% scale CRM65 wing [19].

Table 3 Pressure tap locations on the 8.9% scale CRM65 wing [19, 21].

Row Number	Orientation	Normalized Spanwise Location*, y/b	Spanwise Location (m), y
1	Normal	0.11	0.16764
2	Streamwise	0.11	0.16764
3	Streamwise	0.28	0.42672
4	Normal	0.44	0.67056
5	Streamwise	0.44	0.67056
6	Normal	0.60	0.91440
7	Streamwise	0.60	0.91440
8	Normal	0.81	1.23444
9	Streamwise	0.81	1.23444
10	Streamwise	0.90	1.37160

*Spanwise location is provided for the leading-edge taps at rows 1, 4, 6, and 8 that were oriented normal to the leading edge.



(a) Curvilinear **(b) Unstructured Voronoi** **(c) Cartesian**

Fig. 3 Comparison of three mesh paradigms for the CRM65 wing with high-fidelity ice (L2). The contour uses a color band to represent the cube root of cell volume. Voronoi and Curvilinear meshes have a gradient within each color band, while Cartesian mesh levels have fixed spacings at each level.

III. Computational Methodology

The LAVA framework [29] is used to perform this computational study. LAVA can handle structured curvilinear, structured Cartesian, and unstructured arbitrary polyhedral meshes. Separate computational fluid dynamics solvers within the framework are used for each type of mesh, namely, LAVA Curvilinear, LAVA Cartesian, and LAVA Unstructured, respectively. Examples of the three different mesh paradigms used for the high-fidelity ice shape at a specific spanwise location are shown in Fig. 3. In this work, the unstructured meshes used are based on Voronoi diagrams and generated using the LAVA Voronoi mesher [32]. Across all meshing strategies, WMLES [33–36] is used to accurately and efficiently resolve the unsteady separated flows involving a range of length scales typical in icing application [10–12, 14]. The WMLES implementation within LAVA evaluates the LES solution all the way to the wall using wall stress and heat flux boundary conditions supplied by the wall model, which provides a stress boundary condition for the LES. The implemented algebraic wall model is an analytical law that smoothly blends the viscous sub-layer and log-layer [10]. The constant-coefficient anisotropic Vreman model is used as the sub-grid scale closure, with a fixed value of 0.07 for all curvilinear simulations and 0.08 for all Voronoi and Cartesian simulations. Additional details regarding the WMLES approach in LAVA can be found in [10, 37, 38]. The explicit third-order total variation diminishing Runge-Kutta scheme [39] is used for time-marching with Courant-Friedrichs-Lewy numbers of 1.5 for the curvilinear simulations and 2 for the Voronoi and Cartesian simulations.

A. Curvilinear

Given the complexity of ice shapes like the high-fidelity ice shape in Fig. 1, it is simply not feasible to construct meshes using conventional body-fitted meshing practices. Therefore, for the curvilinear paradigm, the wing without ice

Table 4 Summary of new unstructured Voronoi meshes. GPUs refer to NVIDIA A100 GPUs. The energy consumption is estimated based on peak power recordings of 800 W per compute node for the FP64 A100 GPU simulations, where each compute node has 4 GPUs.

Ice Shape	Mesh Name	Cells (million)	Minimum Δx (mm)	Averaged Δt (s)	Number of GPUs used	Wall-clock hours per CTU	Megajoules per CTU
HiFi	L4	22	0.4	3.222×10^{-7}	4	1.14	3.27
HiFi	L2	97	0.2	1.530×10^{-7}	16	1.95	22.41
Smooth	L2	90	0.2	1.641×10^{-7}	32	0.80	18.48
Smooth	L1	445	0.1	0.817×10^{-7}	64	3.99	183.86
Smooth	L05	470	0.05	0.345×10^{-7}	128	5.28	486.79

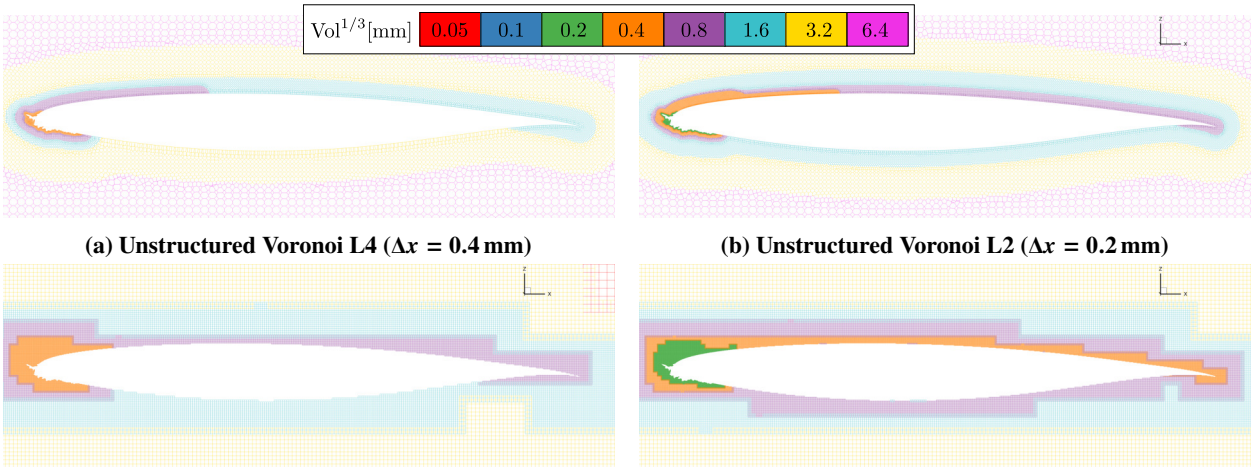
is meshed using standard body-fitted techniques and the effect of the ice on the flow is enforced implicitly with penalty terms added to the governing equations using a source-term-based immersed-boundary method [10, 11, 40–45]. The specific source-term immersed-boundary method used is formulated as a Brinkman penalization [46]. Additional details regarding this penalty approach as implemented in LAVA can be found in [10, 11, 44]. For the spatial discretization, the convective flux derivatives are expressed in terms of numerical flux functions at the half-points [37] and are evaluated using a second-order KEEP-type scheme [11, 47]. Specifically, the KEEP-Scale approach outlined in [47] is used. Standard second-order accurate central differencing is used for the discretization of the viscous fluxes [37].

A new mesh was constructed and results are compared to those in [11]. In contrast to [11] that included the circular splitter plate and the tunnel floor at a location of $y = -0.0635$ m, here the splitter plate is excluded and a symmetry plane is placed at $y = 0$, consistent with the unstructured Voronoi simulations in [11, 14]. Another difference with the new mesh is that the spanwise spacing near the ice is finer and equal to 0.2 mm due to the sensitivity to spanwise mesh spacing noted in [11]. The finer spanwise spacing corresponds to the off-wall spacing. With these modifications, the new mesh, denoted "Improved Mesh" in the numerical results, has 608.6 million nodes.

B. Unstructured Voronoi

The unstructured solver uses a second-order finite-volume method for spatial discretizations on arbitrary polyhedral meshes. Further details regarding the general numerical discretization are provided in [38], and specific details regarding the KEEP convective flux discretization are provided in [11]. For the unstructured solver, Voronoi-type meshes are constructed with the LAVA Voronoi mesher [32]. Voronoi meshes are advantageous because they can be generated in an automated fashion that removes the manual overhead associated with generating body-fitted curvilinear meshes [32, 38]. They also have isotropic cells that are ideal for WMLES and lead to an explicit representation of the ice within the mesh in the current context, which avoids sensitivities associated with immersed-boundary-type methods. In this work, new Voronoi meshes for both ice shapes were constructed and compared to those in [11]. Table 4 summarizes the characteristics of the constructed Voronoi meshes, along with some of the simulation parameters including computational cost. Here, CTU denotes "convective time units", where a single convective time unit is equal to the mean aerodynamic chord (MAC), defined in Table 2, divided by the freestream velocity magnitude, defined in Table 1. It is important to note that energy consumption is sensitive to the number of GPUs used to perform a simulation and the wall-clock hours it takes to simulate one CTU. Comparing the energy consumption numbers reported here in Tables 4 and 5 with those in [30] highlights these sensitivities. The main features distinguishing the new meshes compared to the authors' previous publication are in several additional distinct refinement regions to more efficiently capture the details of the iced geometry leading to reduced cell counts while maintaining the same minimum cell size near the ice, the use of the Geomagic-fixed triangulations as opposed to the shrink-wrapped triangulations, and the generation of finer meshes for the smooth ice to better capture the flow behavior near the leading edge. Fig. 4 depicts the refinement regions for the high-fidelity ice shape on L2 and L4 levels. In addition separate meshes for the more challenging smooth ice geometry which has a smooth-body separation problem are shown in Fig. 5.

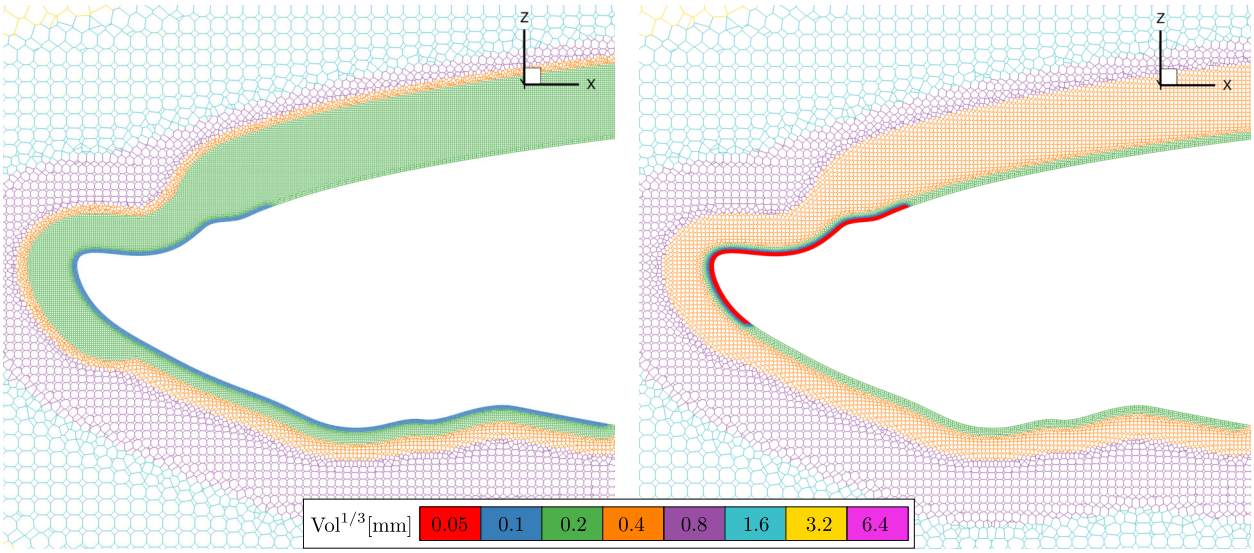
All unstructured Voronoi meshes generated for the current work, except for the L05 mesh level used for smooth ice shape, obey the same description for refinement regions relative to a single length scale parameter (L_s) that allows the creation of these progressively refined families of meshes. For these meshes, the base cell size distribution is created by using telescoping regions that become two times coarser as they move away from the surface, each of them with a



(a) Unstructured Voronoi L4 (Δx = 0.4 mm) **(b) Unstructured Voronoi L2 (Δx = 0.2 mm)**

(c) Cartesian L4 (Δx = 0.4 mm) **(d) Cartesian L2 (Δx = 0.2 mm)**

Fig. 4 Comparison of mesh resolutions L2 and L4 for high-fidelity ice shape between unstructured Voronoi and structured Cartesian approach at row 3 (y/b = 0.28).



(a) Unstructured Voronoi L1 (Δx = 0.1 mm) **(b) Unstructured Voronoi L05 (Δx = 0.05 mm)**

Fig. 5 Comparison of meshing strategies for L1 and L05 unstructured Voronoi meshes for smooth ice at y/b = 0.28 (Row 3). Refinement for the L05 mesh is localized to the smooth body separated flow region near the leading edge.

thickness corresponding to 8-cells of height. The relative size of the first layer was chosen to be $4L_s$ on the top of the iced wing and $8L_s$ on its bottom. Additionally, targeted refinement areas were added to the base cell distribution. A single 8-cell-height layer with $2L_s$ was added up to 30% of the chord on the upper side of the wing only. Moreover, two constant thickness regions with $2L_s$ cell spacing were included, one 4 mm-thick region near the upper portion of the iced horn and one 7.5 mm-thick region above the wing, from the up to 10% of its chord. Finally, a region with a variable thickness equivalent to 4 cells of height with unitary relative length scale was added near the horn ice. These cell size distributions can be observed in the L4, L2, and L1 unstructured meshes for both high-fidelity and smooth ice shapes shown in Figs. 4 and 5, respectively.

After obtaining results on the smooth ice configuration with the L2 and L1 mesh levels with the previously described cell distribution strategy, it was decided to concentrate the location of the most refined cells to the upper portion of the

Table 5 Summary of Cartesian meshes. GPUs refers to NVIDIA A100 GPUs. The energy consumption is estimated based on peak power recordings of 800 W per compute node for the FP64 A100 GPU simulations, where each compute node has 4 GPUs.

Ice Shape	Mesh Name	Solve Cells (million)	Minimum Δx (mm)	Averaged Δt (s)	Number of GPUs used	Wall-clock hours per CTU	Megajoules per CTU
HiFi	L4	79.3	0.4	5.146×10^{-7}	16	0.21	2.45
HiFi	L2	334.7	0.2	2.317×10^{-7}	32	0.94	21.63
Smooth	L2	273.8	0.2	2.285×10^{-7}	16	0.86	9.91
Smooth	L1	718.8	0.1	1.209×10^{-7}	32	2.52	58.06

horn ice accretion and to decrease the off-body refinement over the upper surface near the leading edge. This decision was made based on sensitivity of the airflow around the iced wing to mesh refinement. Ultimately, the L05 mesh was designed to have the same cell size distribution of the L1 mesh with two exceptions: the constant thickness regions were set to have an absolute cell size of 0.4 mm instead of 0.2 mm and the horn ice refinement was restricted to the upper portion of the ice with an 8-cell-thick layer of 0.05 mm spacing. The effect of these adjustments are exhibited in Fig. 5.

C. Cartesian

Details on the WMLES implementation in LAVA Cartesian are provided in Cadieux and Barad [48]. In this work, for the convective flux discretization, a second-order accurate KEEP scheme designed to match that of the LAVA unstructured solver [11] and a fourth-order accurate hybrid central-upwind extension of the scheme described in [48] are compared. The latter scheme is denoted as "CENQ". The Cartesian simulation set-up, like that for curvilinear and Voronoi, uses a free-air configuration with a symmetry plane at $y = 0$. The farfield is located 50 m in the positive and negative streamwise directions and 100 m in the spanwise direction from the wing root. With this domain, Cartesian nonconforming meshes using refinement ratios of 2 are generated with an automated approach. A base forest of octrees, where the leaves are boxes of 8^3 Cartesian cells, is generated to cover the domain, and the boxes are refined into 8 children and their parent discarded until the user-specified mesh spacing for various regions is reached. Table 5 summarizes the meshes used in this work, along with some of the simulation parameters including computational cost. Meshes with minimum cell size of 0.4 mm and 0.2 mm were generated for the high-fidelity ice and finer meshes with minimum size of 0.2 mm and 0.1 mm were generated for the smooth ice. In both cases, a cylinder region immediately aft of the ice shape was tagged for refinement to the finest level present in the mesh to better capture the separated shear layer induced by the ice shape. In Table 5, the cell counts, wall-clock hours per CTU, and energy consumption per CTU are largely dependent on the refinement region immediately aft of the ice shape and can be significantly reduced with more judicious refinement, e.g., with Cartesian adaptive mesh refinement.

IV. Numerical Results and Discussion

Numerical results are compiled for the CRM65 wing for all three mesh paradigms in LAVA with high-fidelity and smooth ice shapes. The simulations are run out until the integrated loads reach a statistically stationary state. Experimental data for comparison is taken from [20–22] and is based on wind-tunnel corrected values as the computational domain does not model the entire wind tunnel. The numerical simulations use the corresponding angles of attack based on the wind-tunnel correction and the aerodynamic moments were taken about the MAC (1/4-chord) location. In [11], some discrepancy was observed between the numerical and experimental aerodynamic moments at the higher angles of attack with the Voronoi method. However, after the publication of [11], further discussions with Brett Bornhoft and the experimentalists revealed that the discrepancy was related to differences between the experimental and numerical methods of computing the moment about the MAC (1/4-chord) location. Specifically, in [11], the experimental moment about the MAC (1/4-chord) location that was compared against was computed as

$$C_{M,\text{MAC (1/4-chord)}} = C_{M,\text{moment center}} - \frac{x_{\text{moment center}} - x_{\text{MAC (1/4-chord)}}}{\text{MAC}} C_L. \tag{1}$$

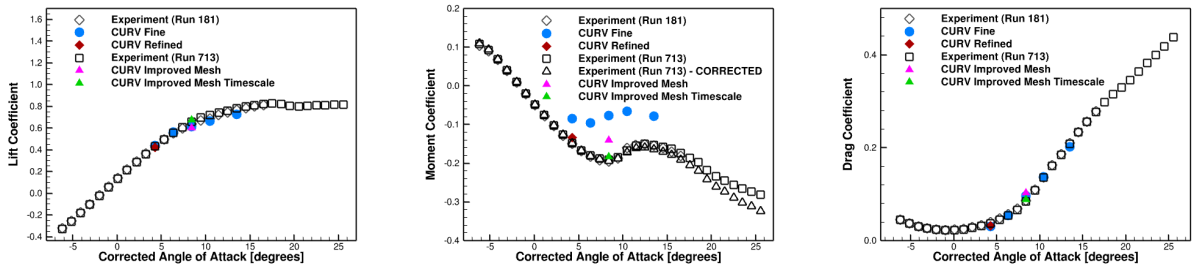


Fig. 6 Aerodynamic loads with Curvilinear solver for the CRM65 wing with high-fidelity leading-edge ice compared to experiment.

However, Eq. (1) can be considered as a special case of the following equation that additionally depends on the angle of attack and drag coefficient:

$$C_{M,\text{MAC (1/4-chord)}} = C_{M,\text{moment center}} - \frac{x_{\text{moment center}} - x_{\text{MAC (1/4-chord)}}}{\text{MAC}} \left(\cos(\alpha)C_L + \sin(\alpha)C_D\right). \tag{2}$$

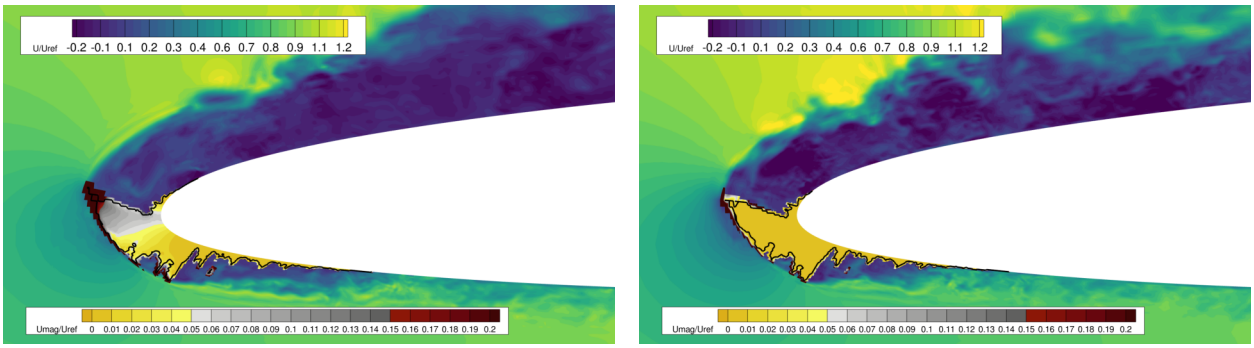
When $\alpha = 0°$, Eq. (2) reduces to Eq. (1). In the present work, the experimental aerodynamic moment about the MAC (1/4-chord) location is evaluated with both Eq. (1) and Eq. (2). The latter equation, Eq. (2), is consistent with how the moment is computed in the numerical simulations and is therefore denoted in the plot legends with the suffix "CORRECTED".

A. High-Fidelity Ice Shape

The high-fidelity ice shape was simulated across a range of angles of attack from 2.185° to 24.524°, depending on the solver. In [11], for the curvilinear method, it was noted that there was significant sensitivity to spanwise mesh spacing where insufficient resolution led to an inability to capture flow through the gaps between the ice shape thus leading to discrepancy with the comparison to the experiment in terms of moment, skin-friction coefficient, and pressure profiles. In this work, the new mesh with finer spanwise spacings was compared to the results in [11] at an angle of attack of 8.423°. The integrated loads for the new mesh, denoted "CURV Improved Mesh" are shown in Fig. 6. With the new mesh, there is relatively little change in lift and drag, but significant improvement in the moment comparison. To address the remaining moment discrepancy, a study was performed investigating the source-term immersed-boundary timescale. From Fig. 7, it can be observed that with a source-term timescale of 145.01×10^{-5} CTU, the implicit representation of the ice is quite porous, allowing up to 15% of the normalized velocity magnitude through the ice. In contrast, when the source-term timescale is reduced to 1.50×10^{-5} CTU, denoted "CURV Improved Mesh Timescale" in the legend, the ice appears much more solid to the flow, and improves the agreement between the numerical and experimental moment values even further, as shown in Fig. 6. In both cases shown in Fig. 7, the timestep size used for the simulations is on the order of 1.50×10^{-5} CTU.

Focusing now on Voronoi and Cartesian results for the high-fidelity ice, Fig. 8 shows integrated loads across a range of angles of attack. Compared to the Voronoi meshes from [11], the new Voronoi meshes (denoted with the suffix "NEW" in the legend) with a reduced number of cells and with the Geomagic-fixed triangulation demonstrate excellent agreement with the experiment. Clearly, the updated moment (denoted with "CORRECTED" in the legend) agrees much better with the computational results and addresses the moment discrepancy between the numerical and experimental values at high angles of attack with unstructured Voronoi identified in [11]. For the Cartesian results, good agreement is obtained at 2.185° and 24.524° with the KEEP scheme; however, at 8.423° and 10.465°, the hybrid central-upwind scheme (CENQ) gives better agreement with the experiment.

Next, flow visualizations with unstructured Voronoi and Cartesian are compared at 8.423°. Figures 9 and 10 give streamwise velocity contours for Voronoi and Cartesian, respectively, for the L2 meshes at several spanwise sections along the wing. For both grid paradigms, the separation increases towards the outboard region of the wing. However, the Cartesian mesh appears to resolve finer structures due to the additional refinement region aft of the ice compared to Voronoi. Figure 11 shows time-averaged and instantaneous skin-friction contours compared to the experimental oil flow with Voronoi and Fig. 12 shows an analogous plot for Cartesian. Examining the time-averaged contours for both solvers, there are streamwise structures near the inboard leading edge portion of the wing similar to what can be observed in the



(a) Source-term timescale: 145.01×10^{-5} CTU **(b) Source-term timescale: 1.51×10^{-5} CTU**

Fig. 7 Instantaneous streamwise velocity normalized by velocity magnitude with Curvilinear solver for the CRM65 wing with high-fidelity leading-edge ice at angle of attack of 8.423° and $y/b = 0.60$ (Row 7) (KEEP scheme, Improved grid).

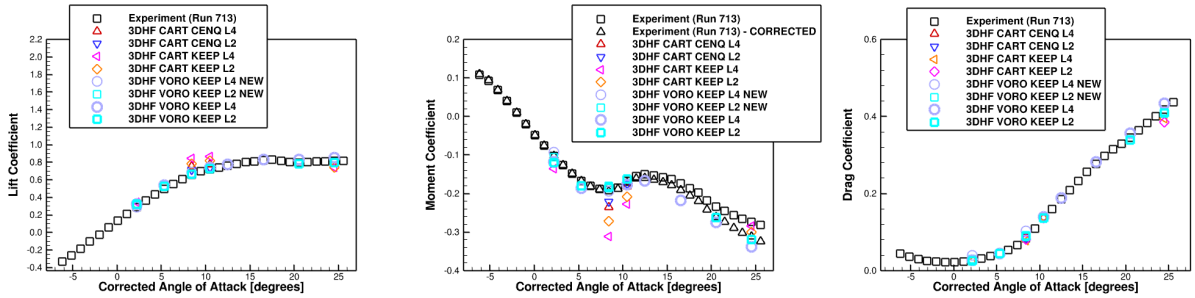


Fig. 8 Aerodynamic loads with Voronoi and Cartesian solvers for the CRM65 wing with high-fidelity leading-edge ice compared to experiment.

oil flow visualization. Near the midboard, there is a region of slightly higher skin-friction that appears to be present for both approaches, but is slightly higher in the case of the Cartesian solver. Figure 13 shows the time-averaged contours across all three solvers. Similar structures are seen across mesh paradigms with the inboard streamwise structures being slightly less pronounced for the curvilinear solver, perhaps due to the source-term ice representation, and the skin-friction is slightly higher in the inboard leading edge and midboard region for Cartesian.

Finally, examining the pressure profiles 2.185° in Fig. 14 shows good agreement between the experiment, Voronoi, and Cartesian results with slight overprediction in upper surface suction for "CART KEEP L4" that is particularly noticeable for rows 9 and 10, but improves on the L2 mesh. Figure 15 shows the pressure profiles across all three mesh paradigms at 8.423°. The Cartesian solver with KEEP scheme has a tendency to overpredict the upper surface suction. This improves with mesh refinement and also when switching to the fourth-order hybrid central-upwind scheme, which trends faster towards the experiment with mesh refinement. The Voronoi profiles agree quite well with the experiment with a slight underprediction in upper surface suction near the leading edge at row 7 that does not seem to improve with refinement. Finally, the curvilinear profiles demonstrate a slight underprediction in upper surface suction towards the outboard portion of the wing. Overall, the pronounced roughness of the high-fidelity ice shape promotes the rapid development of turbulent flow over the wing, making it well-suited for WMLES to capture across all three mesh paradigms.

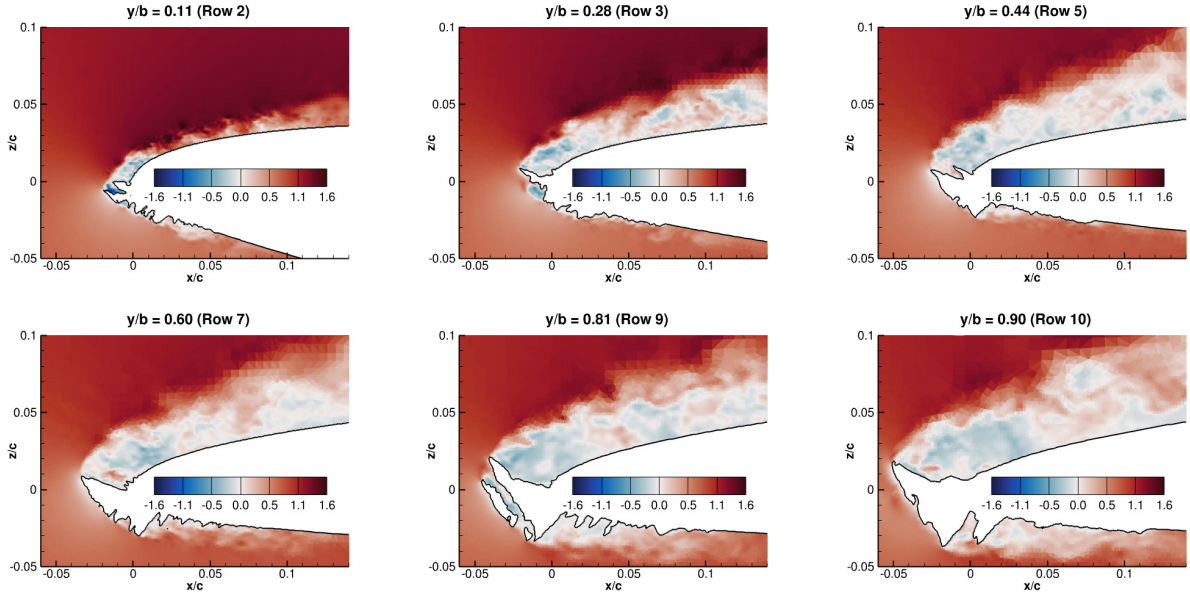


Fig. 9 Instantaneous streamwise velocity normalized by velocity magnitude with unstructured Voronoi for the CRM65 wing with high-fidelity leading-edge ice at angle of attack of 8.423° (KEEP scheme, L2 grid).

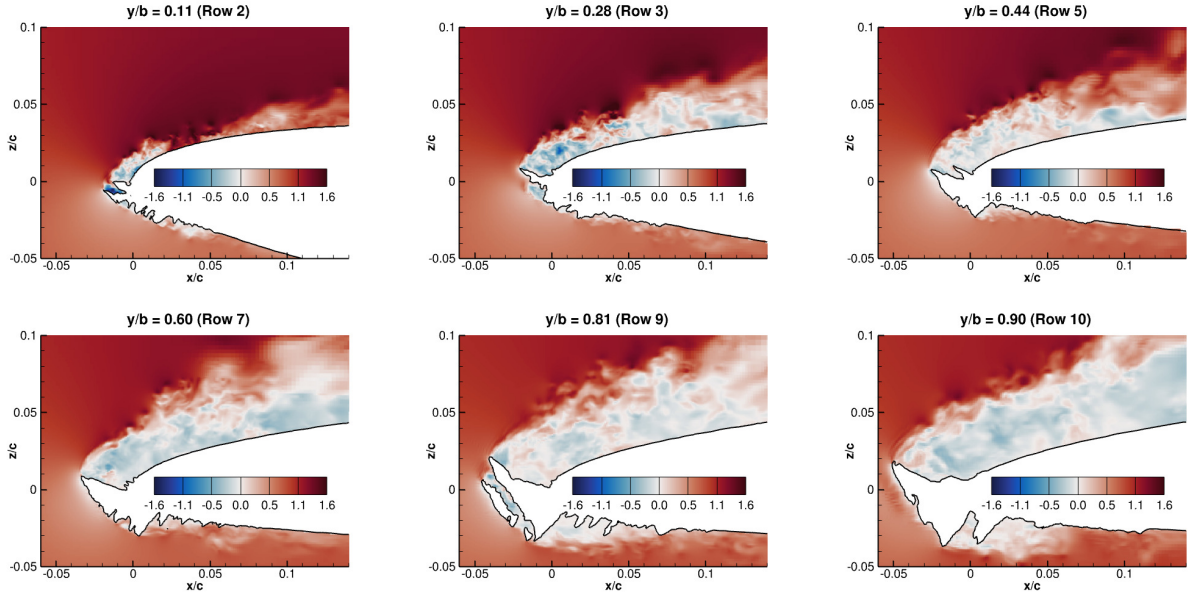
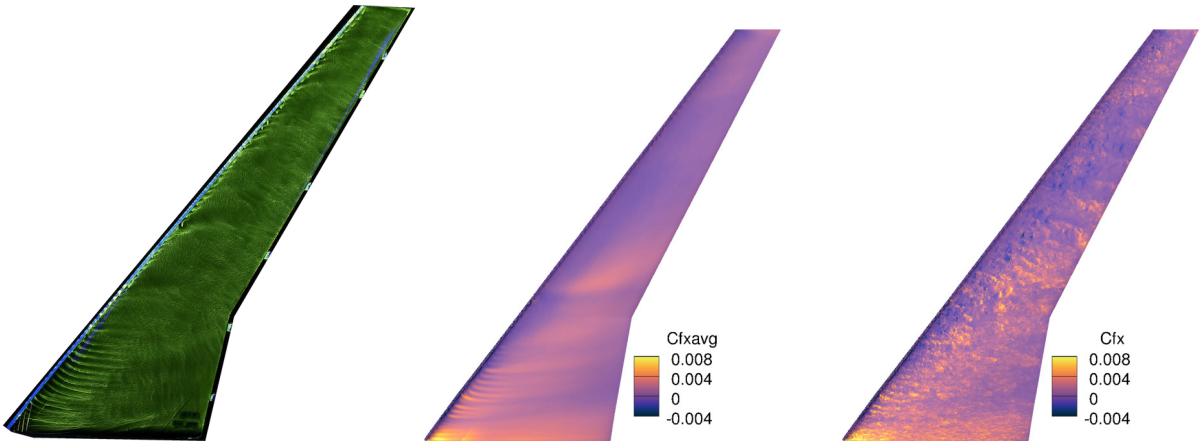
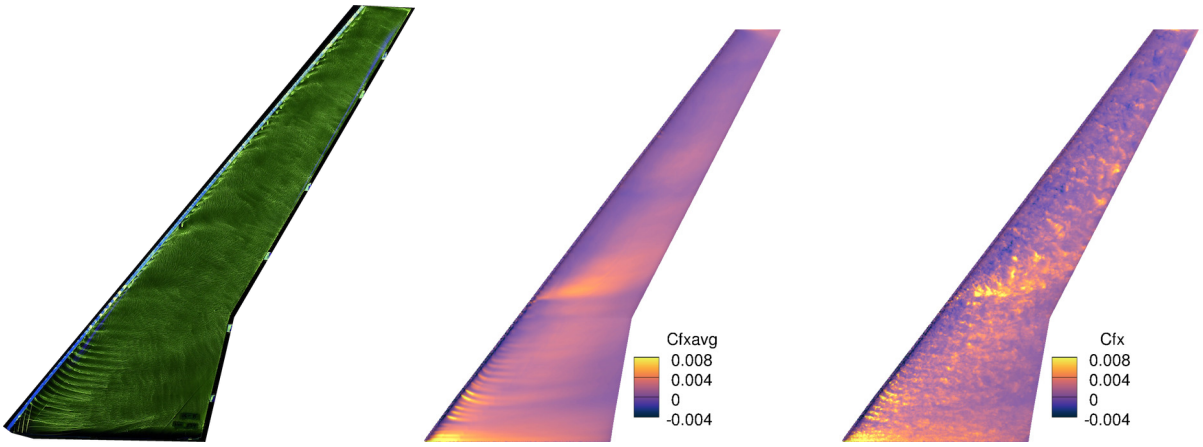


Fig. 10 Instantaneous streamwise velocity normalized by velocity magnitude with Cartesian for the CRM65 wing with high-fidelity leading-edge ice at angle of attack of 8.423° (CENQ scheme, L2 grid).



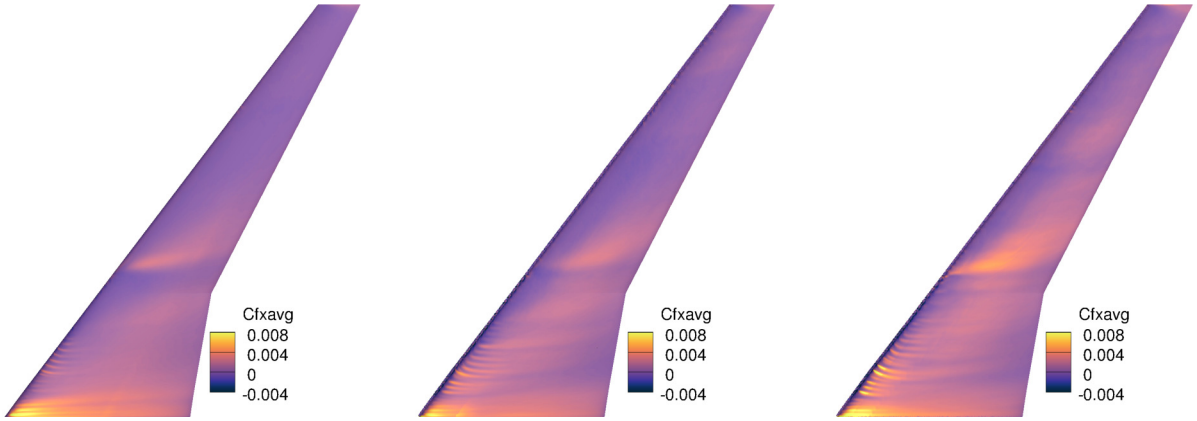
(a) Oil flow visualization (b) Time-averaged skin-friction (c) Instantaneous skin-friction

Fig. 11 Experimental oil flow visualization compared to contours of time-averaged and instantaneous coefficient of skin-friction with unstructured Voronoi for the CRM65 wing with high-fidelity leading-edge ice at angle of attack of 8.423° (KEEP scheme, L2 grid).



(a) Oil flow visualization (b) Time-averaged skin-friction (c) Instantaneous skin-friction

Fig. 12 Experimental oil flow visualization compared to contours of time-averaged and instantaneous coefficient of skin-friction with Cartesian for the CRM65 wing with high-fidelity leading-edge ice at angle of attack of 8.423° (CENQ scheme, L2 grid).



(a) Curvilinear **(b) Voronoi** **(c) Cartesian**

Fig. 13 Contours of time-averaged coefficient of skin-friction with Curvilinear (KEEP scheme, Improved grid), Voronoi (KEEP scheme, L2 grid), and Cartesian (CENQ scheme, L2 grid) solvers for the CRM65 wing with high-fidelity leading-edge ice at angle of attack of 8.423°.

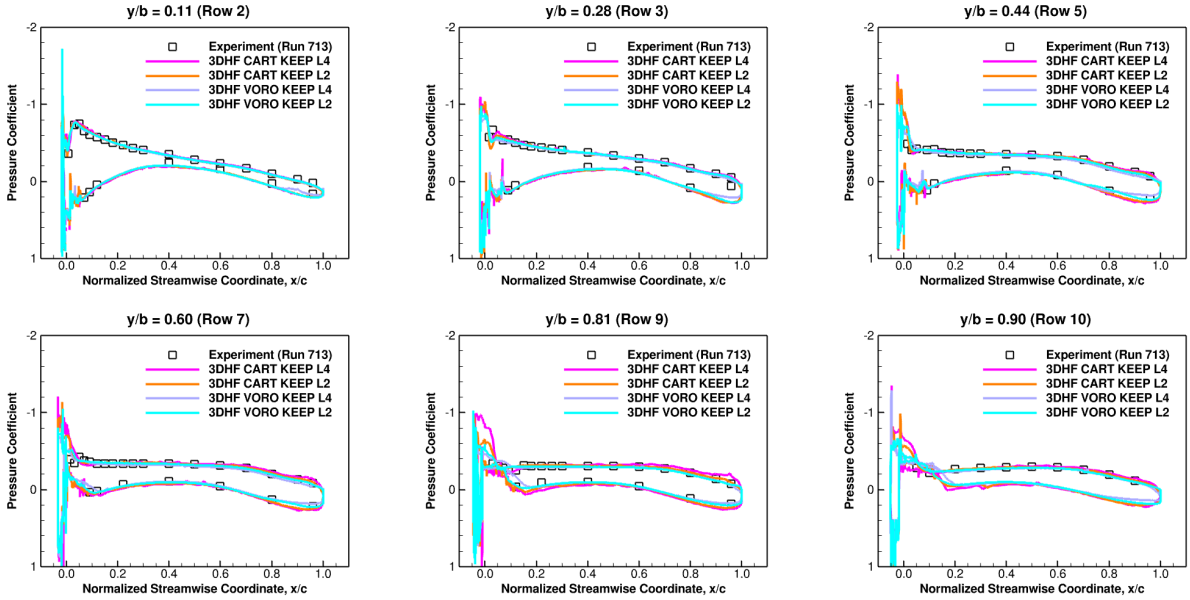


Fig. 14 Time-averaged coefficient of pressure with Voronoi and Cartesian solvers for the CRM65 wing with high-fidelity leading-edge ice at angle of attack of 2.185° compared to experiment.

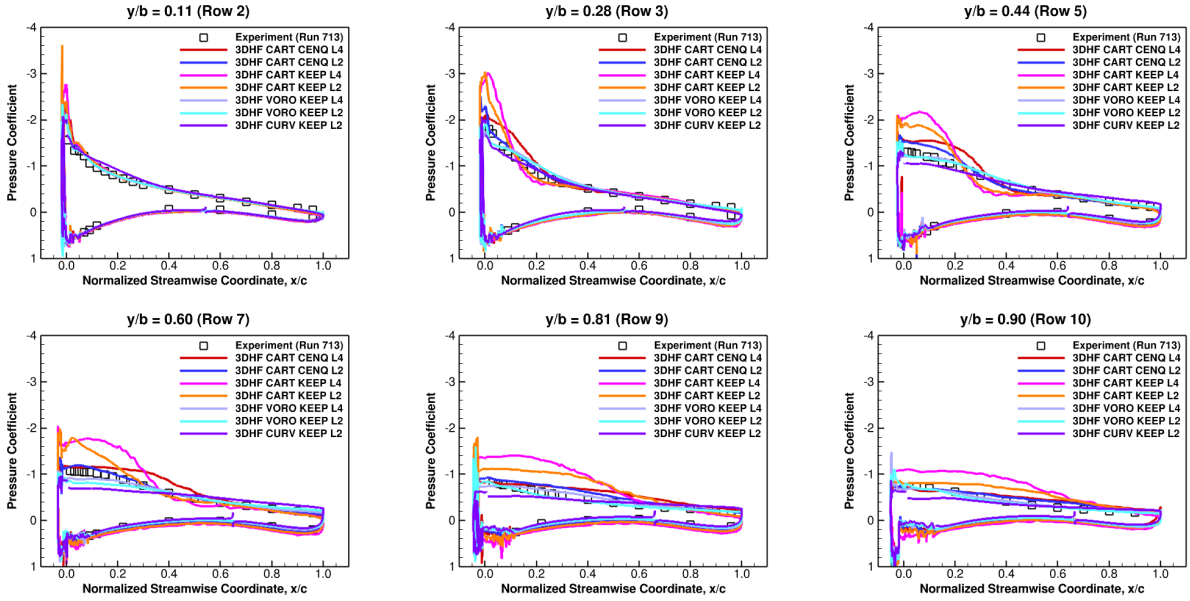


Fig. 15 Time-averaged coefficient of pressure with curvilinear, unstructured Voronoi, and Cartesian for the CRM65 wing with high-fidelity leading-edge ice at angle of attack of 8.423° compared to experiment.

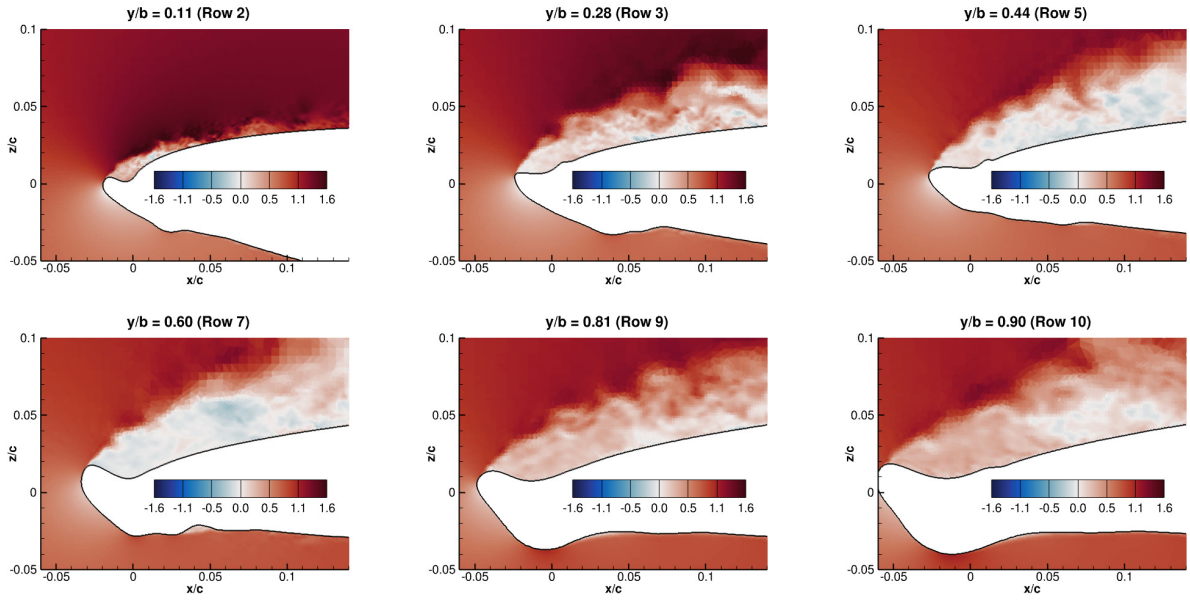


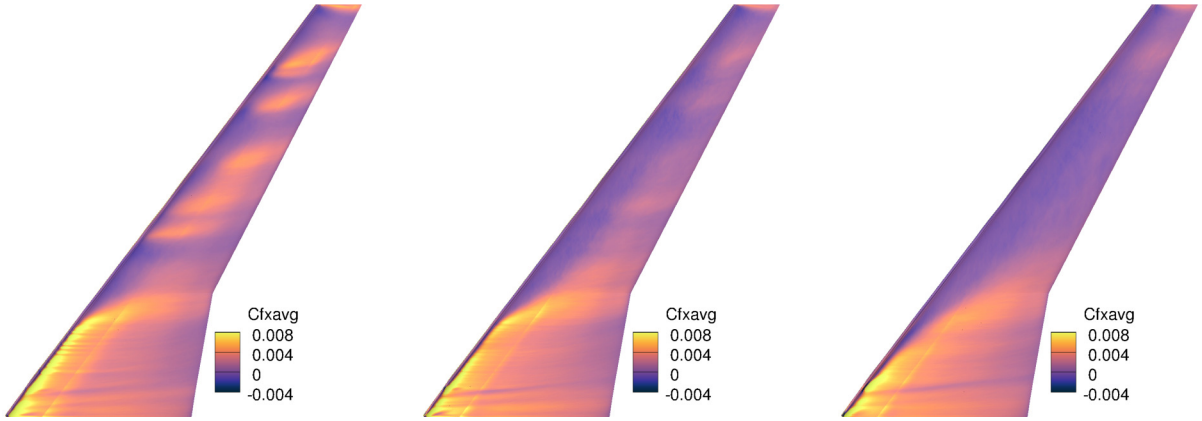
Fig. 16 Instantaneous streamwise velocity normalized by velocity magnitude with unstructured Voronoi for the CRM65 wing with smooth leading-edge ice at angle of attack of 8.458° (KEEP scheme, L05 grid).

B. Smooth Ice Shape

Here, the CRM65 wing with smooth ice is studied at an angle of attack of 8.458°. Results with the Voronoi and Cartesian meshes for the smooth ice summarized in Tables 4 and 5, respectively, are compared to curvilinear and Voronoi results from Craig Penner et al. [11] and Voronoi results from Bornhoft et al. [14]. In [14], the smooth ice was hypothesized to introduce laminar boundary layers and laminar-to-turbulent transition effects, due to the lack of substantial leading-edge roughness present for the high-fidelity ice. This was addressed by introducing additional mesh resolution near the leading-edge and modeling the smooth ice with a no-slip boundary condition, which lead to good agreement with the experiment at 8.458° at the cost of 1.2 billion mesh cells and a reduced timestep [14]. This work follows a similar strategy in an attempt to improve upon the results for the smooth ice presented in [11].

To begin the investigation, Fig. 16 shows contours of instantaneous streamwise velocity normalized by freestream velocity magnitude for unstructured Voronoi on the finest mesh considered (L05). Comparing the velocity contours for the smooth ice in Fig. 16 to velocity contours for the high-fidelity ice in Fig. 9 shows that there is significantly less negative velocity immediately aft of the smooth ice, which confirms that the flow topology for the smooth ice is fundamentally distinct from the high-fidelity ice. Figure 17 shows the behavior of time-averaged surface skin-friction with mesh refinement and Fig. 18 shows corresponding profiles at several stations along the span to give a sense of how the flow topology changes with mesh refinement. Notably, there is an initial drop in skin-friction near the leading edge and it moves further upstream with mesh refinement. Figure 19 shows the variation in the x/c location of the initial drop in skin-friction with refinement at inboard, midboard, and outboard stations that reinforces this trend. Figure 20 compares the upper-surface y^+ profiles for the L1 and L05 unstructured Voronoi meshes. For the L05 mesh, the y^+ values are below five near the leading edge and within the laminar sublayer of the boundary layer, which falls withing the wall-resolved LES regime.

To analyze the leading-edge flow further, Figs. 21 and 22 show the flow behavior near the leading edge under mesh refinement with unstructured Voronoi near inboard ($y/b = 0.11$) and outboard ($y/b = 0.81$) stations, respectively. At the inboard station, three primary flow features were identified that vary with refinement: a drop in skin friction (A), recirculation (B), and boundary layer re-establishment (C). Examining the trends with increasing refinement indicates that the drop in skin-friction (A) moves upstream, the recirculation region (B) moves downstream, and the re-establishment of the boundary layer (C) becomes more gradual. At the outboard station, the leading-edge flow is characterized by an initial separation corresponding to a sudden drop in skin-friction (A), followed by a recirculation region (B). With increasing refinement, the initial separation point (A) moves upstream and the recirculation region (B) decreases in size.



(a) L2 mesh **(b) L1 mesh** **(c) L05 mesh**

Fig. 17 Comparison of contours of time-averaged skin-friction with unstructured Voronoi across three mesh levels for the CRM65 wing with smooth leading-edge ice at angle of attack of 8.458° (KEEP scheme).

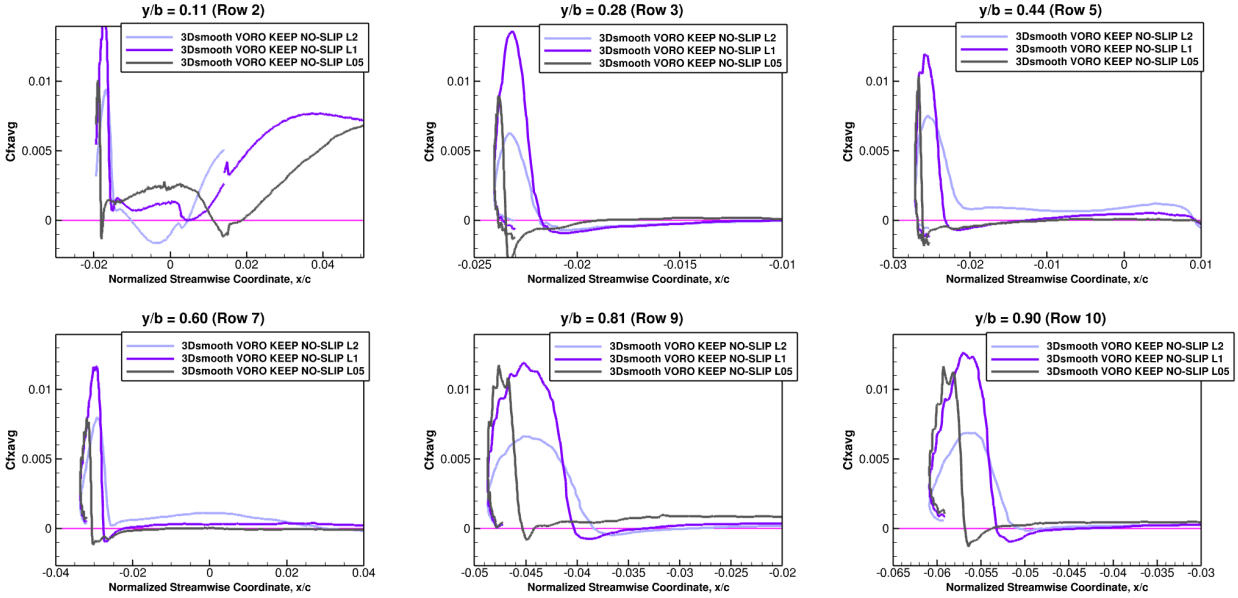


Fig. 18 Time-averaged upper-surface skin-friction profiles with unstructured Voronoi for the CRM65 wing with smooth leading-edge ice at angle of attack of 8.458°. The horizontal magenta lines denote Cfxavg = 0.

Figure 23 shows the integrated loads compared to experiment. The data denoted by "3Dsmooth VORO KEEP L4" is taken from [11] for comparison. There is little spread across the different methods in lift and drag, and agreement with the experiment is reasonable. However, there is more discrepancy between the numerical and experimental results for the moment. Examining the pressure profiles in Fig. 24 shows that the Cartesian KEEP approach produces a large overprediction in upper surface suction that is reduced both with mesh refinement and when switching to the fourth-order CENQ scheme. The Voronoi method also produces an overprediction in upper surface suction, similar to [11], but trends towards the experiment with mesh refinement. Specifically, the L05 mesh with Voronoi KEEP approaches the experiment with reduced upper surface suction overprediction, while the curvilinear profile from [11] underpredicts upper surface suction along the span. Figure 25 compares the Voronoi pressure profiles to the "Fine" and "XXFine" Voronoi results from Bornhoft et al. [14]. The agreement between the present L05 profiles and the XXFine profiles of [14] is excellent. Notably, the L05 mesh in the present work has only 470 million cells compared to the XXFine mesh in [14] that has 1.2 billion cells. However, the timestep size is also a significant contributer to computational cost, and is

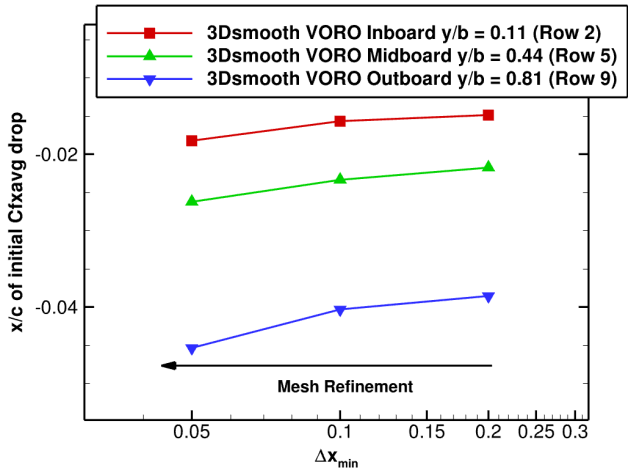


Fig. 19 Variation in x/c location of initial drop in time-averaged upper-surface skin-friction with unstructured Voronoi for the CRM65 wing with smooth leading-edge ice at angle of attack of 8.458°.

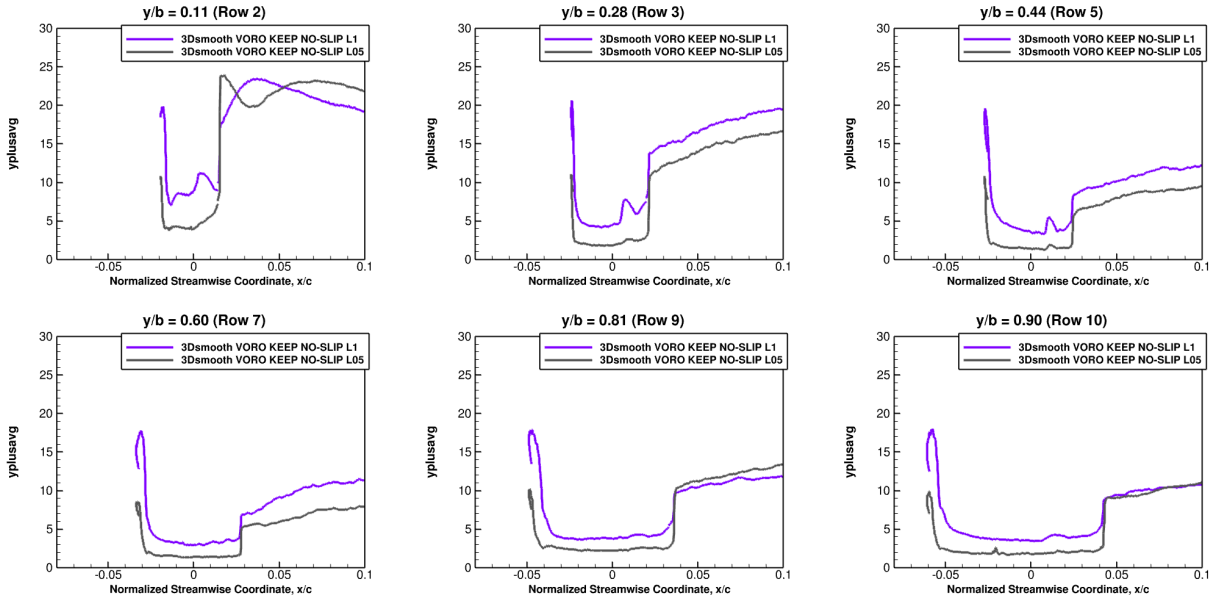
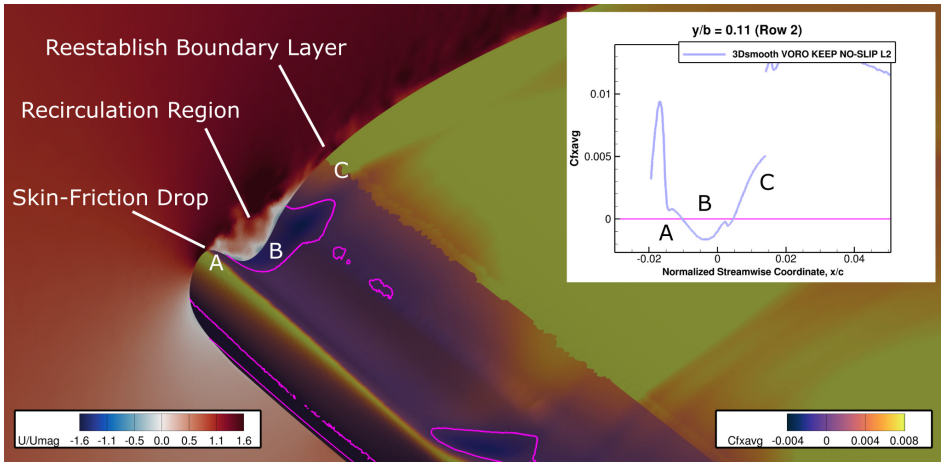
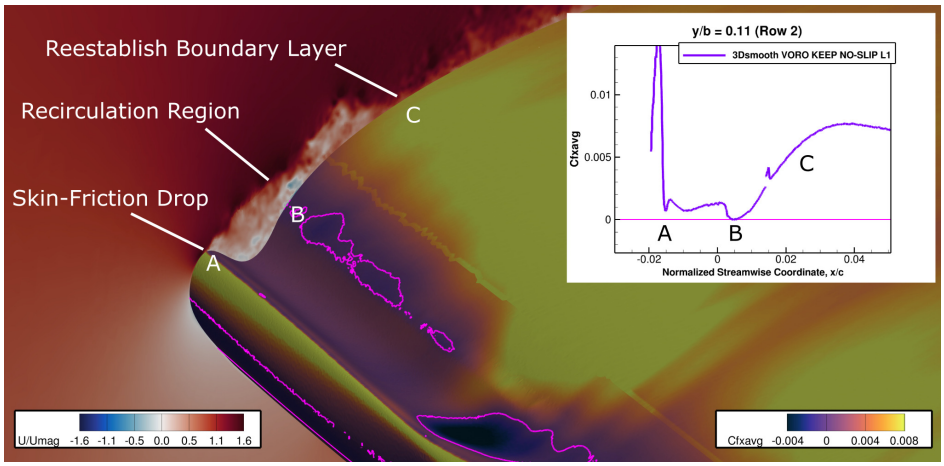


Fig. 20 Time-averaged upper-surface y^+ profiles with unstructured Voronoi for the CRM65 wing with smooth leading-edge ice at angle of attack of 8.458°.

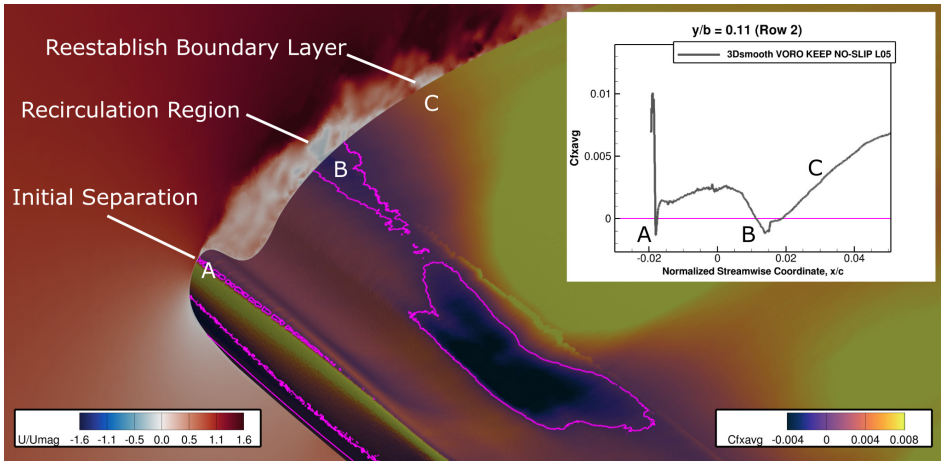
likely similar in for both the XXFine mesh in [14] and the present L05 mesh given that the minimum cell size is the same for both meshes. Finally, Fig. 26 shows that the skin-friction contours on the L05 mesh reproduce several features present in the experimental oil flow visualization.



(a) L2 mesh

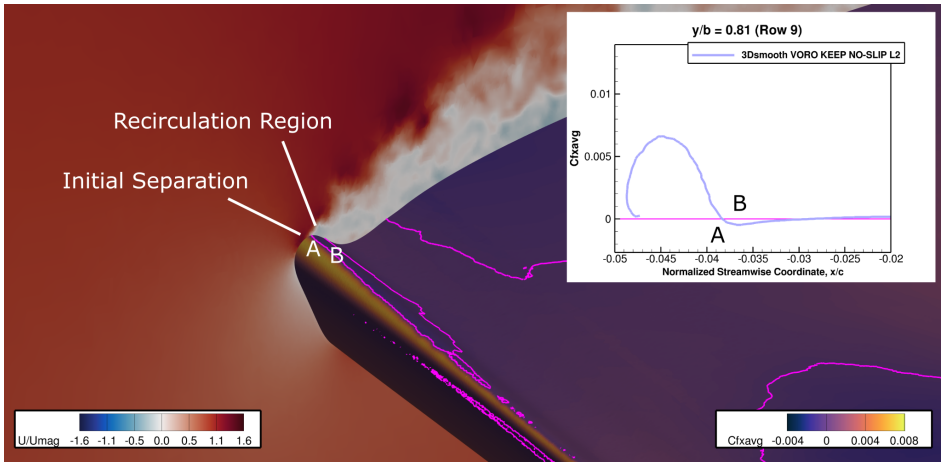


(b) L1 mesh

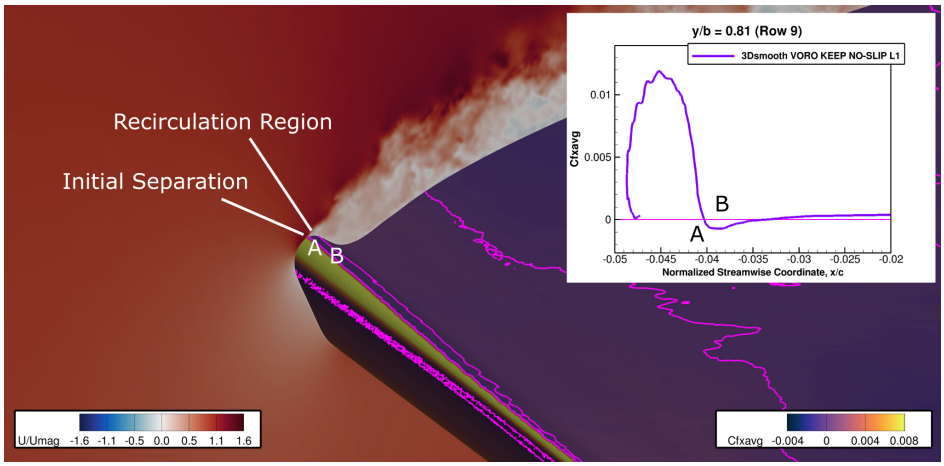


(c) L05 mesh

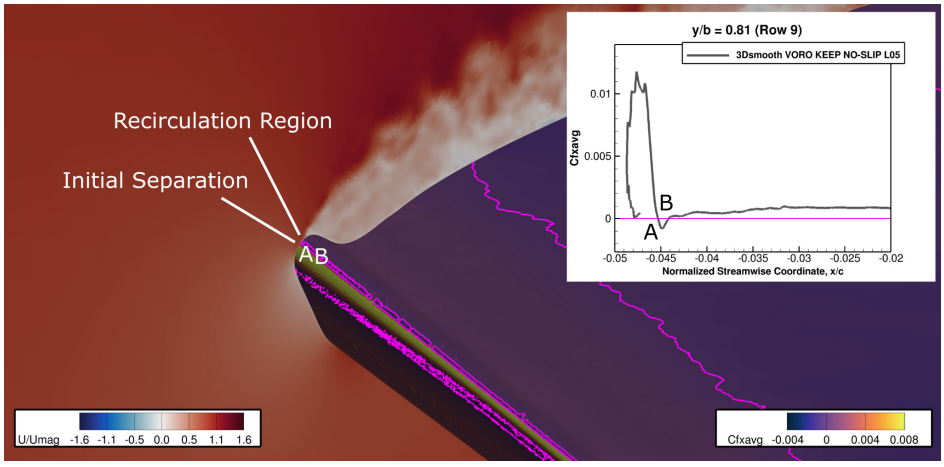
Fig. 21 Flow behavior near the leading edge under mesh refinement with unstructured Voronoi for the CRM65 wing with smooth leading-edge ice at angle of attack of 8.458°. Time-averaged contours of skin-friction coefficient are shown on the surface, where the magenta lines correspond to Cfxavg = 0. Instantaneous streamwise velocity contours are shown on a slice at $y/b = 0.11$. The inset shows time-averaged skin-friction profiles.



(a) L2 mesh



(b) L1 mesh



(c) L05 mesh

Fig. 22 Flow behavior near the leading edge under mesh refinement with unstructured Voronoi for the CRM65 wing with smooth leading-edge ice at angle of attack of 8.458°. Time-averaged contours of skin-friction coefficient are shown on the surface, where the magenta lines correspond to Cfxavg = 0. Instantaneous streamwise velocity contours are shown on a slice at $y/b = 0.81$. The inset shows time-averaged skin-friction profiles.

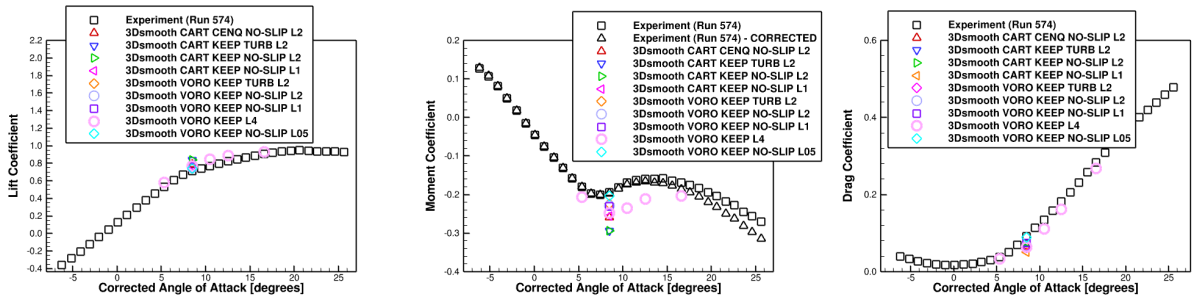


Fig. 23 Aerodynamic loads with unstructured Voronoi and Cartesian for the CRM65 wing with smooth leading-edge ice compared to experiment.

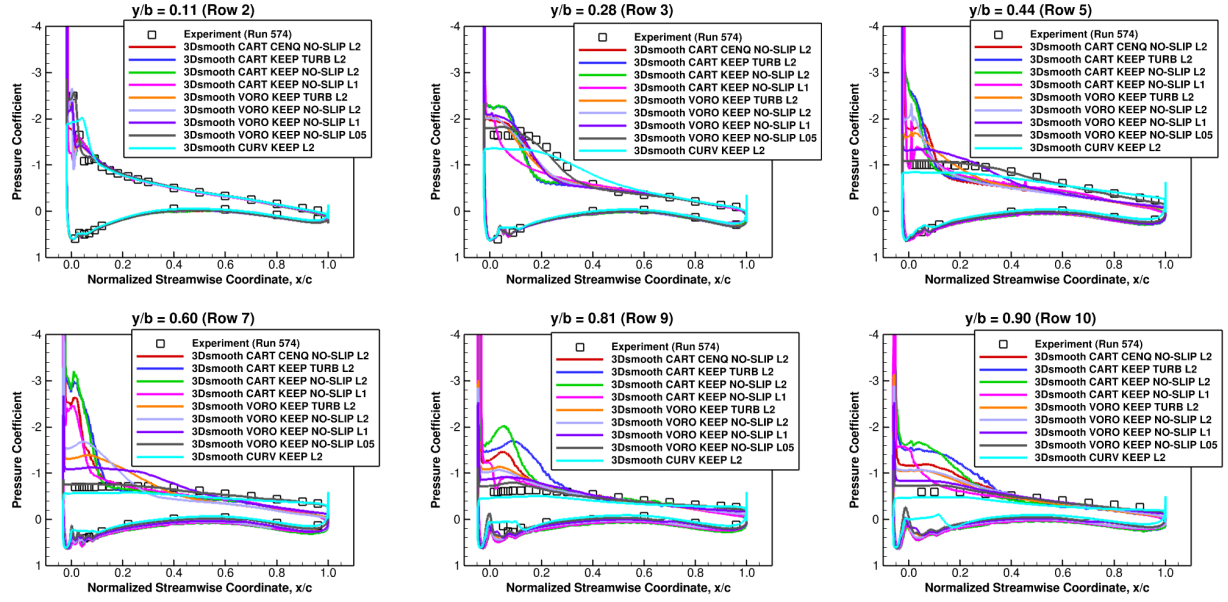


Fig. 24 Time-averaged coefficient of pressure with curvilinear, unstructured Voronoi, and Cartesian for the CRM65 wing with smooth leading-edge ice at angle of attack of 8.458° compared to experiment.

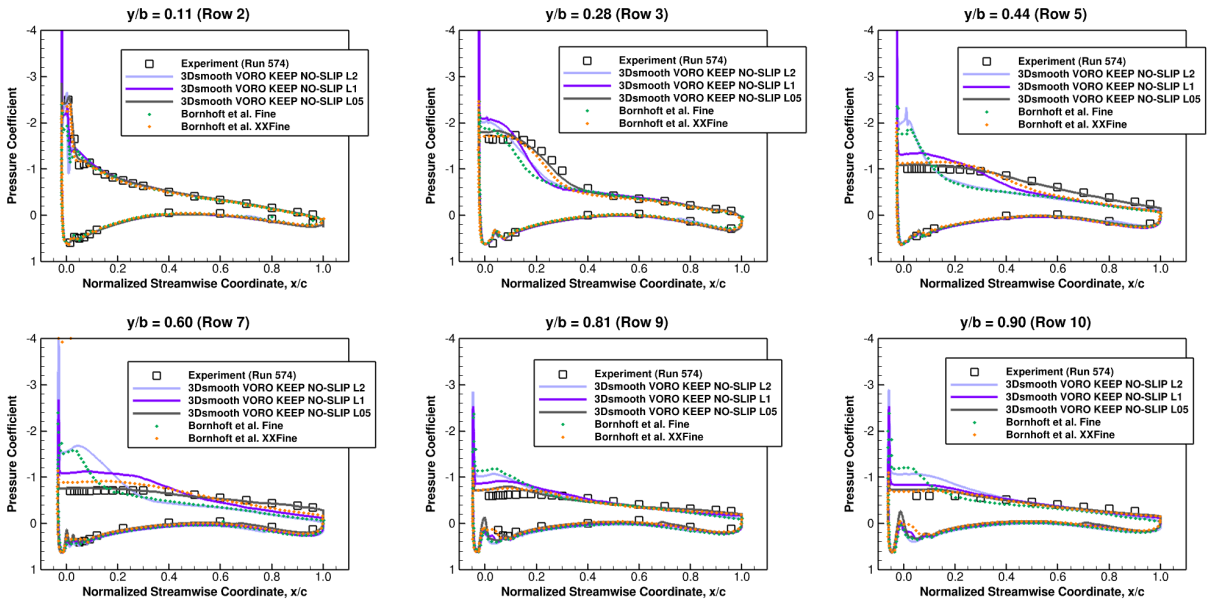
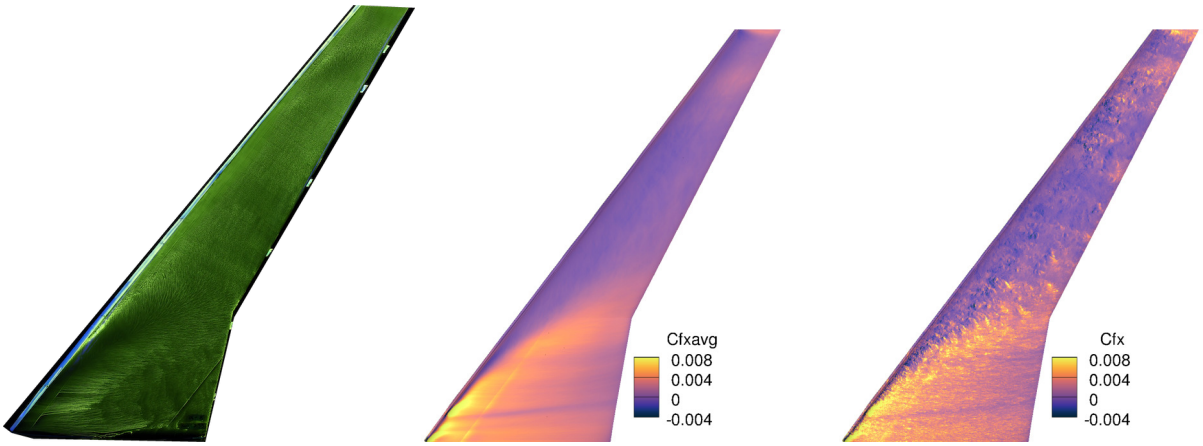


Fig. 25 Time-averaged coefficient of pressure with unstructured Voronoi for the CRM65 wing with smooth leading-edge ice at angle of attack of 8.458° compared to experiment and results from Bornhoft et al. [14].



(a) Oil flow visualization **(b) Time-averaged skin-friction** **(c) Instantaneous skin-friction**

Fig. 26 Experimental oil flow visualization compared to contours of time-averaged and instantaneous coefficient of skin-friction with unstructured Voronoi for the CRM65 wing with smooth leading-edge ice at angle of attack of 8.458° (KEEP scheme, L05 grid).

V. Summary and Conclusions

This study evaluated WMLES of a swept wing with high-fidelity and smooth leading-edge ice shapes using three distinct mesh paradigms—structured curvilinear overset, unstructured Voronoi, and Cartesian—implemented within the LAVA framework. The findings demonstrated the strengths and limitations of each strategy while providing valuable insights into the aerodynamic effects of in-flight icing and predictive capabilities of WMLES.

For the high-fidelity ice shape, good agreement was achieved across the three mesh paradigms. However, the curvilinear strategy demonstrated significant sensitivity to the source-term timescale, a parameter in the hybrid body-fitted/source-term immersed-boundary method that controls how effectively the ice geometry is represented as a solid boundary. When the timescale is too large, the representation of the ice becomes porous, allowing flow through the geometry which leads to inaccuracies in predicting aerodynamic loads and flow separation. This sensitivity highlighted the importance of carefully tuning the source-term timescale to achieve reliable predictions. In contrast, the Voronoi and Cartesian methods avoid this sensitivity as they either explicitly mesh the ice geometry or employ a ghost-cell immersed-boundary approach that directly enforces the no-penetration boundary condition based on the underlying geometry. These latter two approaches inherently capture the physical behavior of the ice without requiring additional parameters like the source-term timescale. In addition, the curvilinear approach requires manual mesh generation, which demands significant expertise from a domain specialist and can add considerable time to the overall solution process, particularly for complex geometries. In contrast, the Cartesian method allows for on-the-fly mesh generation, often completing in minutes, while the Voronoi approach can generate meshes for complex iced geometries within a few hours. This is a dramatic improvement over the manual mesh generation required for the curvilinear approach, which often takes several days to weeks depending on the complexity of the geometry. Between the latter two methods, the Cartesian approach exhibited some sensitivity to the choice of numerical flux scheme, requiring careful selection to achieve optimal accuracy; however, both Cartesian and Voronoi methods showed convergence toward experimental results with increased mesh refinement.

For the smooth ice configuration, the results underscored the challenges posed by the laminar boundary layers and transition effects introduced by the lack of substantial leading-edge roughness. Mesh refinement, especially with the unstructured Voronoi paradigm, led to significant improvements, bringing numerical predictions closer to experimental data in terms of integrated loads, pressure profiles, and skin-friction contours. The Cartesian approach showed similar behavior to Voronoi in terms of a large overprediction of upper-surface suction near the leading edge, but this behavior improved with mesh refinement. Notably, for the Voronoi method, refinement led to significant improvements when the upper-surface y^+ values near the leading edge fell within the laminar sublayer, further enhancing agreement with experimental observations. These findings are consistent with those presented by Bornhoft et al. [14].

Future work will focus on addressing these challenges by testing different modeling approaches to better capture the laminar-to-turbulent flow behavior observed with the smooth ice shape. Forced transition will also be applied to coarser meshes, using the transition location identified in the L05 results as a guide, to evaluate its effectiveness in reducing computational costs while maintaining accuracy. Additional refinement strategies will be explored, including comparing the effects of localized 0.5 mm mesh refinement with broader, more global refinement. Furthermore, a finer Cartesian mesh with enhanced localized refinement will be generated to examine its impact on resolving flow features more accurately at reduced computational cost. Lastly, as the smooth ice geometry is less complex, a fully meshed curvilinear grid will be created to evaluate its performance in capturing flow characteristics associated with the smooth ice configuration. To further enhance the understanding of iced aerodynamics predictions, additional configurations will be simulated, incorporating varying geometries and conditions, while actively collaborating with experimentalists to validate findings and improve the physical fidelity of the simulations.

Acknowledgments

We gratefully acknowledge funding from NASA's Aeronautics Research Mission Directorate (ARMD) through the Transformational Tools and Technologies (TTT) Project via the Revolutionary Computational Aerosciences (RCA) technical challenge and the Advanced Air Transport Technology (AATT) Project. We extend our gratitude to Andy Broeren, Sam Lee, and the AATT Project Team from NASA's John H. Glenn Research Center for providing the wing geometry, ice triangulations, and experimental data, in addition to insightful discussions. We acknowledge Brett Bornhoft for sharing his expertise in using Geomagic for pre-processing the ice triangulations and helpful discussions. We are grateful to the LAVA Team for helpful discussions and code development, particularly Emre Sozer for developing the LAVA Unstructured solver. Computational resources supporting this work were provided by the NASA High-End Computing (HEC) Program through the NASA Advanced Supercomputing (NAS) Division at Ames Research Center. Finally, we acknowledge Chase Ashby and Chris DeGrendele for internal review.

References

[1] Struk, P., Broeren, A., Potapczuk, M., Kreeger, R. E., Blankenship, K., Chen, R.-C., Flegel, A., Porter, C., Ratvasky, T., Van Zante, D., Van Zante, J., Bedka, K., Harrah, S., Smith, J. G., Wohl, C., Tsao, J.-C., Work, A., and Bragg, M., "NASA Analysis of Alternatives Study for Icing Research," Tech. Rep. NASA/TM-20220006956, National Aeronautics and Space Administration, Glenn Research Center, Cleveland, Ohio 44135, 2022. URL `https://ntrs.nasa.gov/citations/20220006956`.

[2] Stebbins, S. J., Loth, E., Broeren, A. P., and Potapczuk, M., "Review of Computational Methods for Aerodynamic Analysis of Iced Lifting Surfaces," *Progress in Aerospace Sciences*, Vol. 111, 2019. https://doi.org/10.1016/j.paerosci.2019.100583.

[3] Pan, J., and Loth, E., "Reynolds-Averaged Navier-Stokes Simulations of Airfoils and Wings with Ice Shapes," *Journal of Aircraft*, Vol. 41, No. 4, 2004, pp. 879–891. https://doi.org/10.2514/1.587.

[4] Chi, X., Li, Y., Addy, H. E., Choo, Y., Shih, T., and Chen, H., "A Comparative Study Using CFD to Predict Iced Airfoil Aerodynamics," *43rd AIAA Aerospace Sciences Meeting and Exhibit*, American Institute of Aeronautics and Astronautics, Reno, NV, 2005. https://doi.org/10.2514/6.2005-1371, AIAA 2005-1371.

[5] Chaouat, B., "The State of the Art of Hybrid RANS/LES Modeling for the Simulation of Turbulent Flows," *Flow, Turbulence and Combustion*, Vol. 99, No. 2, 2017, pp. 279–327. https://doi.org/10.1007/s10494-017-9828-8.

[6] Rumsey, C. L., Slotnick, J. P., and Sclafani, A. J., "Overview and Summary of the Third AIAA High Lift Prediction Workshop," *Journal of Aircraft*, Vol. 56, No. 2, 2019, pp. 621–644. https://doi.org/10.2514/1.C034940.

[7] Rumsey, C. L., Slotnick, J. P., and Woeber, C. D., "Fourth High-Lift Prediction/Third Geometry and Mesh Generation Workshops: Overview and Summary," *Journal of Aircraft*, 2023, pp. 1–18. https://doi.org/10.2514/1.C037168.

[8] Xiao, M., Zhang, Y., and Zhou, F., "Numerical Study of Iced Airfoils with Horn Features using Large-Eddy Simulation," *Journal of Aircraft*, Vol. 56, No. 1, 2019, pp. 94–107. https://doi.org/10.2514/1.C034986.

[9] Xiao, M., Zhang, Y., and Zhou, F., "Numerical Investigation of the Unsteady Flow Past an Iced Multi-Element Airfoil," *AIAA Journal*, Vol. 58, No. 9, 2020, pp. 3848–3862. https://doi.org/10.2514/1.J059114.

[10] Wong, M. L., Ghate, A. S., Stich, G.-D., Kenway, G. K., and Kiris, C. C., "Numerical Study on the Aerodynamics of an Iced Airfoil with Scale-Resolving Simulations," *AIAA SCITECH 2023 Forum*, American Institute of Aeronautics and Astronautics, National Harbor, MD & Virtual, 2023. https://doi.org/10.2514/6.2023-0252, AIAA 2023-0252.

[11] Craig Penner, D. A., Housman, J. A., Stich, G.-D., Sousa, V. C. B., Koch, J. R. L., and Duensing, J. C., "Wall-Modeled Large-Eddy Simulations of a Swept Wing With Leading-Edge Ice," *AIAA AVIATION 2024 Forum*, American Institute of Aeronautics and Astronautics, Las Vegas, NV, 2024. https://doi.org/10.2514/6.2024-3999, AIAA 2024-3999.

[12] Bornhoft, B., Jain, S. S., Goc, K., Bose, S. T., and Moin, P., "Large-Eddy Simulations of the NACA23012 Airfoil with Laser-Scanned Ice Shapes," *Aerospace Science and Technology*, Vol. 146, 2024. https://doi.org/10.1016/j.ast.2024.108957.

[13] Wong, M. L., Ghate, A. S., Kenway, G. K., Angel, J. B., and Kiris, C. C., "Immersed Boundary Wall-Modelled Large Eddy Simulations of Straight Wings With Three-Dimensional Ice Accretion," *AIAA AVIATION 2024 Forum*, American Institute of Aeronautics and Astronautics, Las Vegas, NV, 2024. https://doi.org/10.2514/6.2024-4000, AIAA 2024-4000.

[14] Bornhoft, B. J., Jain, S. S., Bose, S. T., and Moin, P., "Large-Eddy Simulations of the CRM65 Swept Wing under Real and Artificial Icing Conditions," *AIAA SCITECH 2024 Forum*, American Institute of Aeronautics and Astronautics, Orlando, FL, 2024. https://doi.org/10.2514/6.2024-1336, AIAA 2024-1336.

[15] Vassberg, J., Dehaan, M., Rivers, M., and Wahls, R., "Development of a Common Research Model for Applied CFD Validation Studies," *26th AIAA Applied Aerodynamics Conference*, American Institute of Aeronautics and Astronautics, Honolulu, HI, 2008. https://doi.org/10.2514/6.2008-6919, AIAA 2008-6919.

[16] Vassberg, J., Tinoco, E., Mani, M., Rider, B., Zickuhr, T., Levy, D., Brodersen, O., Eisfeld, B., Crippa, S., Wahls, R., Morrison, J., Mavriplis, D., and Murayama, M., "Summary of the Fourth AIAA CFD Drag Prediction Workshop," *28th AIAA Applied Aerodynamics Conference*, American Institute of Aeronautics and Astronautics, Chicago, IL, 2010. https://doi.org/10.2514/6.2010-4547, AIAA 2010-4547.

[17] Rivers, M., and Dittberner, A., "Experimental Investigations of the NASA Common Research Model (Invited)," *28th AIAA Applied Aerodynamics Conference*, American Institute of Aeronautics and Astronautics, Chicago, IL, 2010. https://doi.org/10.2514/6.2010-4218, AIAA 2010-4218.

[18] Rivers, M., and Dittberner, A., "Experimental Investigations of the NASA Common Research Model in the NASA Langley National Transonic Facility and NASA Ames 11-Ft Transonic Wind Tunnel (Invited)," *49th AIAA Aerospace Sciences Meeting including the New Horizons Forum and Aerospace Exposition*, American Institute of Aeronautics and Astronautics, Orlando, FL, 2011. https://doi.org/10.2514/6.2011-1126, AIAA 2011-1126.

[19] Broeren, A. P., Woodard, B., Diebold, J. M., and Moens, F., "Low-Reynolds Number Aerodynamics of an 8.9% Scale Semispan Swept Wing for Assessment of Icing Effects," *9th AIAA Atmospheric and Space Environments Conference*, American Institute of Aeronautics and Astronautics, Denver, CO, 2017. https://doi.org/10.2514/6.2017-4372, AIAA 2017-4372.

[20] Lee, S., Broeren, A. P., Woodard, B., Lum, C. W., and Smith, T. G., "Comparison of Iced Aerodynamic Measurements on Swept Wing from Two Wind Tunnels," *2018 Atmospheric and Space Environments Conference*, American Institute of Aeronautics and Astronautics, Atlanta, GA, 2018. https://doi.org/10.2514/6.2018-3493, AIAA 2018-3493.

[21] Broeren, A. P., Lee, S., Woodard, B. S., and Bragg, M. B., "Effect of Geometric Fidelity on the Aerodynamics of a Swept Wing with Glaze Ice Accretion," *AIAA AVIATION 2020 Forum*, American Institute of Aeronautics and Astronautics, Virtual Event, 2020. https://doi.org/10.2514/6.2020-2846, AIAA 2020-2846.

[22] Broeren, A. P., Lee, S., Bragg, M. B., Woodard, B. S., Radenac, E., and Moens, F., "Experimental and Computational Icing Simulation for Large Swept Wings," Tech. Rep. DOT/FAA/TC-22/43, NASA/TP-20210023843, NASA Glenn Research Center and HX5, LLC and University of Washington and University of Illinois at Urbana-Champaign and Office National d'Etudes et de Recherches Aérospatiales. Toulouse, France, 2023. https://doi.org/10.21949/1524516.

[23] Woodard, B. S., and Bragg, M. B., "Effect of Spanwise Discontinuities on the Aerodynamics of a Swept Wing with Scalloped Ice Accretion," *AIAA AVIATION 2020 Forum*, American Institute of Aeronautics and Astronautics, Virtual Event, 2020. https://doi.org/10.2514/6.2020-2848, AIAA 2020-2848.

[24] Fujiwara, G. E., Bragg, M. B., Camello, S., and Lum, C., "Computational and Experimental Ice Accretions of Large Swept Wings in the Icing Research Tunnel," *8th AIAA Atmospheric and Space Environments Conference*, American Institute of Aeronautics and Astronautics, Washington, D.C., 2016. https://doi.org/10.2514/6.2016-3734, AIAA 2016-3734.

[25] Radenac, E., "Validation of a 3D Ice Accretion Tool on Swept Wings of the SUNSET2 Program," *8th AIAA Atmospheric and Space Environments Conference*, American Institute of Aeronautics and Astronautics, Washington, D.C., 2016. https://doi.org/10.2514/6.2016-3735, AIAA 2016-3735.

[26] Stebbins, S. J., Loth, E., and Qin, C., "Computations of Swept Wing Icing Aerodynamics," *AIAA SCITECH 2019 Forum*, American Institute of Aeronautics and Astronautics, San Diego, CA, 2019. https://doi.org/10.2514/6.2019-0328, AIAA 2019-0328.

[27] Stebbins, S., Loth, E., Broeren, A., Potapczuk, M., and Porter, C., "Aerodynamics of a Common Research Model Wing with Leading-Edge Ice Shape," *Journal of Aircraft*, Vol. 58, No. 4, 2021, pp. 894–906. https://doi.org/10.2514/1.C036188.

[28] Ozcer, I., Pueyo, A., Menter, F., Hafid, S., and Yang, H., "Numerical Study of Iced Swept-Wing Performance Degradation using RANS," *International Conference on Icing of Aircraft, Engines, and Structures*, SAE International, Vienna, AT, 2023. https://doi.org/10.4271/2023-01-1402, SAE 2023-01-1402.

[29] Kiris, C. C., Housman, J. A., Barad, M. F., Brehm, C., Sozer, E., and Moini-Yekta, S., "Computational Framework for Launch, Ascent, and Vehicle Aerodynamics (LAVA)," *Aerospace Science and Technology*, Vol. 55, 2016, pp. 189–219. https://doi.org/10.1016/j.ast.2016.05.008.

[30] Sozer, E., Barad, M. F., Housman, J. A., Cadieux, F., Sousa, V. C. B., Dumlupinar, E., Saurabh, K., Ravikumar, K., and Duensing, J., "LAVA WMLES Results for the 5th High-Lift Prediction Workshop," *AIAA SCITECH 2025 Forum*, American Institute of Aeronautics and Astronautics, Orlando, FL, 2025.

[31] "Geomagic Wrap 3D Scanning and Surfacing Software," https://oqton.com/geomagic-wrap/, 2024.

[32] Sousa, V. C., Rodgers, A. K., Sriram, K., Sozer, E., Barad, M. F., Stich, G.-D., Cadieux, F., and Duensing, J. C., "LAVA Voronoi Mesher for Wall-Modeled Large-Eddy Simulations," *AIAA AVIATION 2024 Forum*, American Institute of Aeronautics and Astronautics, Las Vegas, NV, 2024. https://doi.org/10.2514/6.2024-4306, AIAA 2024-4306.

[33] Piomelli, U., and Balaras, E., "Wall-Layer Models for Large-Eddy Simulations," *Annual Review of Fluid Mechanics*, Vol. 34, No. 1, 2002, pp. 349–374. https://doi.org/10.1146/annurev.fluid.34.082901.144919.

[34] Piomelli, U., "Wall-Layer Models for Large-Eddy Simulations," *Progress in Aerospace Sciences*, Vol. 44, No. 6, 2008, pp. 437–446. https://doi.org/10.1016/j.paerosci.2008.06.001.

[35] Larsson, J., Kawai, S., Bodart, J., and Bermejo-Moreno, I., "Large Eddy Simulation with Modeled Wall-Stress: Recent Progress and Future Directions," *Mechanical Engineering Reviews*, Vol. 3, No. 1, 2016. https://doi.org/10.1299/mer.15-00418.

[36] Bose, S. T., and Park, G. I., "Wall-Modeled Large-Eddy Simulation for Complex Turbulent Flows," *Annual Review of Fluid Mechanics*, Vol. 50, 2018, pp. 535–561. https://doi.org/10.1146/annurev-fluid-122316-045241.

[37] Kiris, C. C., Ghate, A. S., Duensing, J. C., Browne, O. M. F., Housman, J. A., Stich, G.-D., Kenway, G. K., Fernandes, L. S., and Machado, L. M., "High-Lift Common Research Model: RANS, HRLES, and WMLES Perspectives for CLmax Prediction using LAVA," *AIAA SCITECH 2022 Forum*, American Institute of Aeronautics and Astronautics, San Diego, CA & Virtual, 2022. https://doi.org/10.2514/6.2022-1554, AIAA 2022-1554.

[38] Sozer, E., Ghate, A. S., Kenway, G. K., Barad, M. F., Sousa, V. C., and Kiris, C. C., "Evaluation of Voronoi Meshes for Large Eddy Simulations of High Lift Aerodynamics," *AIAA SCITECH 2023 Forum*, American Institute of Aeronautics and Astronautics, National Harbor, MD & Virtual, 2023. https://doi.org/10.2514/6.2023-0255, AIAA 2023-0255.

[39] Shu, C.-W., and Osher, S., "Efficient Implementation of Essentially Non-Oscillatory Shock-Capturing Schemes, II," *Journal of Computational Physics*, Vol. 83, No. 1, 1989, pp. 32–78. https://doi.org/10.1016/0021-9991(89)90222-2.

[40] Mohd-Yusof, J., "Combined Immersed-Boundary/B-Spline Methods for Simulations of Flows in Complex Geometries," *Annual Research Briefs, Center for Turbulence Research*, 1997, pp. 317–328. URL https://web.stanford.edu/group/ctr/ResBriefs97/myusof.pdf.

[41] Fadlun, E., Verzicco, R., Orlandi, P., and Mohd-Yusof, J., "Combined Immersed-Boundary Finite-Difference Methods for Three-Dimensional Complex Flow Simulations," *Journal of Computational Physics*, Vol. 161, No. 1, 2000, pp. 35–60. https://doi.org/10.1006/jcph.2000.6484.

[42] Mochel, L., Weiss, P.-É., and Deck, S., "Zonal Immersed Boundary Conditions: Application to a High-Reynolds-Number Afterbody Flow," *AIAA Journal*, Vol. 52, No. 12, 2014, pp. 2782–2794. https://doi.org/10.2514/1.J052970.

[43] Weiss, P.-É., and Deck, S., "On the Coupling of a Zonal Body-Fitted/Immersed Boundary Method with ZDES: Application to the Interactions on a Realistic Space Launcher Afterbody Flow," *Computers & Fluids*, Vol. 176, 2018, pp. 338–352. https://doi.org/10.1016/j.compfluid.2017.06.015.

[44] Lowe, B. M., Ashby, C. P., Koch, J. R. L., Craig Penner, D. A., Housman, J. A., and Duensing, J. C., "Towards Aerodynamic Shape Optimization Using an Immersed Boundary Overset Grid Method," *AIAA AVIATION 2024 Forum*, American Institute of Aeronautics and Astronautics, Las Vegas, NV, 2024. https://doi.org/https://doi.org/10.2514/6.2024-4229, AIAA 2024-4229.

[45] Stich, G.-D., Martin, O. G., Ashby, C., Housman, J. A., and Duensing, J., "Noise Prediction of Multi-Stream Internally Mixed Jets With External and Internal Plugs Using Large-Eddy Simulation," *AIAA SCITECH 2024 Forum*, American Institute of Aeronautics and Astronautics, 2024. https://doi.org/10.2514/6.2024-3377, AIAA 2024-3377.

[46] Angot, P., Bruneau, C.-H., and Fabrie, P., "A Penalization Method to Take Into Account Obstacles in Incompressible Viscous Flows," *Numerische Mathematik*, Vol. 81, No. 3, 1999, pp. 497–520. https://doi.org/10.1007/s002110050401.

[47] Craig Penner, D. A., Housman, J. A., Stich, G.-D., Koch, J. R. L., and Duensing, J. C., "Wall-Modeled Large-Eddy Simulations of a Swept Wing," *AIAA SCITECH 2024 Forum*, American Institute of Aeronautics and Astronautics, Orlando, FL, 2024. https://doi.org/10.2514/6.2024-2376, AIAA 2024-2376.

[48] Cadieux, F., and Barad, M., "Wall-Modeled Large-Eddy Simulation of Supersonic Parachute Inflation," *Eleventh International Conference on Computational Fluid Dynamics (ICCFD11)*, Kobe, Japan, 2024. URL https://iccfd.org/iccfd12/assets/pdf/papers/ICCFD12_Paper_2-A-04.pdf, ICCFD12-2024-C000159.